Nanoscale Advances

ROYAL SOCIETY OF CHEMISTRY

REVIEW

View Article Online
View Journal

Cite this: DOI: 10.1039/d6na00167j

Synthesis of activated carbons and nanoparticle-loaded activated carbons derived from bio-wastes for the removal of ibuprofen drug from water

Ngoc Dung Lai[ab] and Thuan Van Tran *[ab]

The widespread use of ibuprofen has led to its presence in various water sources. Along with the alarmingly increasing residual amount of ibuprofen in water, the long-term exposure of ibuprofen can have negative impacts on humans. Hence, the development of adsorbents to remove ibuprofen from water is necessary. Here, we discuss the synthesis of activated carbons and magnetic activated carbons derived from bio-wastes for the removal of ibuprofen. Typically, the surface area (S_{BET}) of zinc chloride-activated carbons derived from bamboo fibers and from *Quercus variabilis* cork was up to 2000 $m^2\ g^{-1}$. The kinetic, isotherm, and thermodynamic models for ibuprofen adsorption were also examined. The pseudo-second-order model (R^2 values of 0.96–0.99) and the Langmuir model (R^2 values of 0.978–0.999) provided the best fit. The maximum ibuprofen adsorption capacity (Q_{max}) achieved was 38–491 mg g^{-1}. Moreover, the regeneration, recyclability, and adsorption mechanisms were elucidated. With high S_{BET} and Q_{max} values, activated carbons and magnetic activated carbons derived from bio-wastes can be used as recyclable and efficient adsorbents for the removal of ibuprofen.

Received 1st March 2026
Accepted 20th April 2026

DOI: 10.1039/d6na00167j

rsc.li/nanoscale-advances

1. Introduction

Ibuprofen is one of the most widely prescribed nonsteroidal anti-inflammatory drugs (NSAIDs). Ibuprofen is chemically designated as (*R*,*S*)-2-(4-(2-methylpropyl)phenyl)propanoic acid and consists of a central benzene ring substituted with a non-polar isobutyl group at the para-position and a polar propionic acid moiety (Fig. S1). This arrangement creates a chiral center (an asymmetric carbon); hence, ibuprofen is often synthesized and commercialized as a racemic mixture.[1] Physicochemically, ibuprofen is a weak acid with a pK_a value of approximately 4.1 to 4.5 (Table S1). This property thus makes ibuprofen's solubility in water highly pH-dependent. Ibuprofen is poorly soluble under acidic conditions (21 mg L^{-1} at 25 °C) but becomes significantly more soluble as pH increases.[2] With a high octanol–water partition coefficient ($\log P \approx 3.97$), it is classified as a highly lipophilic compound (Table S1).

The extensive use of ibuprofen in pain and inflammation treatment results in its widespread release into water bodies primarily through improper disposal and excretion.[3–5] Therefore, this has resulted in frequent ibuprofen detection in surface waters, groundwater, and even drinking water supplies.[6,7] The persistence of ibuprofen in these ecosystems poses significant risks, such as possible endocrine disruption in aquatic life and long-term human health effects due to bioaccumulation.[8,9] This increasing contamination emphasizes the necessity for dealing with pharmaceutical residues to protect ecosystems and public health. As a result, it is necessary to apply treatment processes for handling these issues.

Conventional wastewater treatment methods, *e.g.*, activated sludge processes,[10] biological treatment,[11] advanced oxidation processes,[12] coagulation–flocculation,[13] electrochemical methods,[14] adsorption,[15] and filtration,[16] were used for the removal of ibuprofen. Among these methods, adsorption is promising, for which biowaste-derived adsorbents, such as activated carbons and magnetic activated carbons, have been regarded as potential candidates. The high surface area, high functional group content, and magnetic susceptibility for separability of biowaste-derived activated adsorbents enhance the adsorption efficiency and reusability.[17–19] Thus, these materials represent alternatives to traditional approaches. This highlights the critical need to develop such materials for effective ibuprofen removal from contaminated water systems.

Converting bio-waste into activated adsorbents is an effective and environmentally friendly strategy for both waste management and water treatment. Substantial quantities of bio-waste, such as crop, fruit, and forest residues, are generated globally.[20,21] Consequently, if the residues are unmanaged, they cause environmental degradation through landfill overburden and methane emissions.[22,23] Transforming these residues into activated adsorbents can mitigate pollution by diverting waste from disposal sites and provide a cost-effective alternative to commercially produced adsorbents. Furthermore, these

[a]Nguyen Tat Thanh University Center for Hi-Tech Development, Saigon Hi-Tech Park, Ho Chi Minh City, Vietnam. E-mail: tranvt@ntt.edu.vn
[b]Institute of Applied Technology and Sustainable Development, Nguyen Tat Thanh University, Ho Chi Minh City, Vietnam

materials often possess high porosity, high surface areas, and surface functional groups, which allow for the efficient adsorption of contaminants, including ibuprofen, from aqueous systems. This approach serves a dual purpose: reducing the environmental burden of waste deposition while producing functional materials for pollutant elimination. As a result, it brings potential solutions of a circular economy.

During the last ten years, there has been an exponential increase in the number of papers published on ibuprofen adsorption employing various activated carbons from 148 articles in 2015 to 1178 articles in 2024, and 565 articles are reported up to April 2025 (Fig. 1). Several studies evaluated ibuprofen adsorption on a range of adsorbents, including carbons, polymers, clays, and metal–organic frameworks.[2] Ayati *et al.* comprehensively reviewed ibuprofen adsorption on carbon materials, *e.g.*, activated biochar, hydrochar, graphene, and multi-walled carbon nanotubes.[24] They also discussed factors influencing the adsorption process and its thermodynamics but largely overlooked the kinetic and isotherm models. In addition, Rashid Ahmed *et al.* mentioned the effect of synthesis conditions and adsorption parameters on biomass-derived biochars for ibuprofen adsorption but not critically scrutinized on adsorption models, optimization, and adsorbent regenerability.[25] However, Esmaeili Nasrabadi *et al.* studied MOFs for the removal of ibuprofen by Pd@MIL-100(Fe), HSO_3-MIL-53(Fe), and UiO-66-MOF with their large pore and rich surface chemistry.[26] Nevertheless, the author did not discuss optimization models, even though these models play a vital role in improving the removal efficiency under optimized conditions. Recently, Ahmad indicated the potential of biowaste-derived activated adsorbents for ibuprofen adsorption and examined kinetic and isotherm models to better understand the adsorption mechanism.[27] Nonetheless, their study had a shortcoming of thermodynamic analysis and optimization. Moreover, the optimization and regeneration studies on the use of activated carbons derived from biowastes for ibuprofen removal were rarely discussed in the literature. Importantly, ibuprofen adsorption mechanisms driven by key interactions, such as H bonding, π–π stacking, and electrostatic attraction, were not comprehensively clarified.

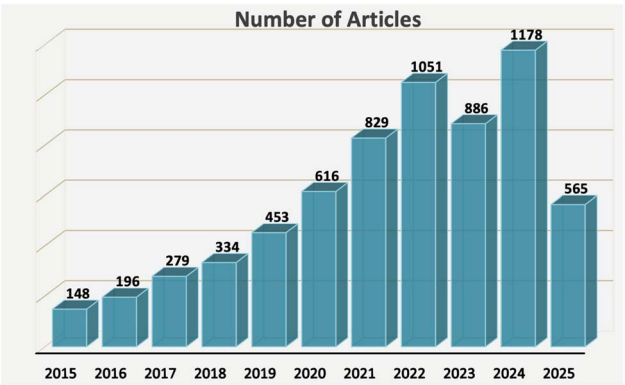

Fig. 1 Annual number of published articles on ibuprofen adsorption using activated carbons from 2015 to April 2025. Data were collected from Scopus using keywords "ibuprofen", "adsorption", and "activated carbon".

This review comprehensively examines the application of biowaste-derived activated adsorbents for ibuprofen remediation, focusing on variants, *e.g.*, magnetic activated carbons that enhance separation and reusability. It addresses the environmental implications of ibuprofen contamination and evaluates the effectiveness of these adsorbents. Additionally, kinetic, isotherm, and thermodynamic models are explored for consideration in terms of discussion in a bid to provide explanations of adsorption processes of activated adsorbents for ibuprofen. Response surface methodology (RSM) optimization is reported to determine the optimal adsorption conditions. Besides, the potential of adsorbent regeneration was reported. This work gives an in-depth overview, calling on researchers to adopt sustainable, waste-to-resource strategies as potential and environmentally friendly options for the treatment of ibuprofen contaminants.

2. Pollution and effect of ibuprofen

2.1. Pollution

Ibuprofen is a widely used NSAID, which has been detected in various aqueous matrices in the globe.[3] Table 1 provides a comprehensive dataset on the occurrence of ibuprofen in rivers, swamps, wetlands, seawater, and wastewater systems. The concentrations of ibuprofen in these water sources exhibit considerable variability. For instance, the concentrations range from trace levels (*e.g.*, < 24 ng L^{-1} in the Ebro Delta seawater)[28] to very high levels (*e.g.*, 3 156 000 ng L^{-1} in the Frio and Oro rivers, Colombia).[29] Notably, the highest levels were found in river systems, specifically in the Frio and Oro rivers in Bucaramanga, Colombia (3 156 000 ng L^{-1}), followed by the São Francisco river in Brazil (785 000 ng L^{-1}),[30] and the Warta river in Poland (496 000 ng L^{-1}).[31] These elevated levels are likely attributable to substantial anthropogenic inputs, such as untreated sewage discharge, industrial effluents, medical wastewater, and runoff from urban and agricultural areas with high ibuprofen usage.[32,33] In contrast, the lowest concentrations were recorded in seawater, such as the Ebro Delta, Spain (limited detection to 24 ng L^{-1}), and the Arctic Archipelago, northern Canada (130–220 ng L^{-1}).[34] The dilution effects in large marine systems and reduced direct human influence in remote regions can be the reasons for the low concentration measurement. This trend suggests that proximity to human activity and the degree of water treatment or dilution are key factors influencing ibuprofen concentrations in aquatic environments.

Globally, river systems have been polluted by a broad range of ibuprofen concentrations. This evaluation indicates the weakening treatment of authorities and the vulnerability of rivers to pharmaceutical pollution. The Frio and Oro rivers in Colombia reported the highest recorded concentration (limited detection to 3 156 000 ng L^{-1}).[29] The author presumed that the inadequate wastewater management and easy accessibility of drugs to the population in Bucaramanga were the causes. Similarly, the São Francisco river in Brazil (limited detection to

Table 1 Pollution of ibuprofen in water sources

Location	Aqueous matrix	Concentration	Ref.
Danube river, Novi Sad, Serbia	River	31–111 ng L^{-1}	35
Frio and Oro rivers, Bucaramanga, Colombia	River	Not detected – 3 156 000 ng L^{-1}	29
Mallorquin swamp, Colombian Caribbean	Swamp	10 000–218 000 ng L^{-1}	36
Albufera Natural Park, on the Mediterranean coast, Spain	Wetland	30–1229 ng L^{-1}	37
São Francisco river, Brazil	River	Not detected – 785 000 ng L^{-1}	30
Warta river, Poland	River	3500–496 000 ng L^{-1}	31
Brazil	Surface waters	7–1700 ng L^{-1}	38
Grombalia Plain, Northeast Tunisia	Ground water	Not detected – 1599 ng L^{-1}	39
Tagus River Basin, Spain	Surface water	5.2–1800 ng L^{-1}	40
Grand River Watershed, Ontario, Canada	Rural sub-watersheds	1200 ng L^{-1}	41
Sewerage system, Sydney, Australia	Sewage water	<1000–13 000 ng L^{-1}	42
River Tame, River Severn, Coventry Canal, and Birmingham and Worcester Canal, Wales	River	Not detected – 256 ng L^{-1}	43
Vhembe and Mopane District Municipalities, Limpopo Province, South Africa	Influent wastewaters	Not detected – 114 000 ng L^{-1}	44
Vhembe and Mopane District Municipalities, Limpopo Province, South Africa	Effluent wastewaters	Not detected – 60 000 ng L^{-1}	44
Subin, Suntreso, and Wiwi rivers in Kumasi Metropolis, Accra, Ghana	Water river	Not detected – 118 000 ng L^{-1}	45
Wastewater treatment plant, Ostrava, Czech Republic	Influent wastewaters	9511–94 054 ng L^{-1}	46
Wastewater treatment plant, Ostrava, Czech Republic	Effluent wastewaters	78–1597 ng L^{-1}	46
Ebro Delta, Spain	Influent wastewaters	11 000–17 452 ng L^{-1}	28
Ebro Delta, Spain	Effluent wastewaters	Not detected – 15 864 ng L^{-1}	28
Ebro Delta, Spain	Seawater	Not detected – 24 ng L^{-1}	28
Arctic Archipelago, northern Canada	Seawater	130–220 ng L^{-1}	34

785 000 ng L^{-1}) and the Warta river in Poland for a period of 2012–2021 (3500–496 000 ng L^{-1}) indicate significant contamination, exacerbated by industrial discharges and untreated sewage inputs over extended periods.[30,31] In Africa, the Subin, Suntreso, and Wiwi rivers in Ghana had a concentration of ibuprofen from limited detection to 118 000 ng L^{-1}, which further illustrated the impact of urban runoff in developing regions.[45] Other rivers, such as the Danube in Serbia (31–111 ng L^{-1}) and the Tagus River Basin in Spain (5.2–1800 ng L^{-1}), showed markedly lower levels, due to better wastewater treatment infrastructure or the strict regulation of authorities.[35,40] The above-mentioned findings indicated higher concentrations in other continents than in Europe. Other studies, for instance, Fekadu *et al.*[47] and Wilkinson *et al.*[48] similarly reported the higher concentration of multi-pharmaceutical products in Africa, North America, and Asia than in Europe. This can be due to the strict regulation on the production, usage, and discharge of pharmaceutical products in Europe. These disparities underscore the role of local environmental management practices and population pressures in determining ibuprofen persistence in rivers.

Swamps and wetlands serve as sinks for ibuprofen pollution, with concentrations varying widely. The Mallorquin swamp in the Colombian Caribbean recorded exceptionally high levels (10 000–218 000 ng L^{-1}), which could be understood due to urban and limited water exchange.[36] In contrast, the Albufera Natural Park wetland in Spain exhibited lower concentrations (30–1229 ng L^{-1}).[37] The lower measured concentration of ibuprofen may be due to the dilution by Mediterranean inflows or natural attenuation through vegetative filtration. Because these ecosystems are characterized by stagnant or slow-moving waters, they tend to accumulate pharmaceuticals from surrounding terrestrial runoff. Ultimately, ibuprofen levels depend on the intensity of upstream human activity and the capacity for natural degradation or sorption to sediments.

Seawater samples typically have the lowest ibuprofen concentrations among the environmental matrices due to the vast dilution capacity of the ocean. In the Ebro Delta, Spain, ibuprofen levels ranged from limited detection to 24 ng L^{-1}, reflecting minimal direct inputs and significant dispersion from terrestrial sources.[28] Similarly, the Arctic Archipelago in northern Canada showed slightly higher concentrations of 130–220 ng L^{-1}.[34] These consistently low values in marine environments suggest that seawater acts as a final diluent for pharmaceutical pollutants, with concentrations diminishing as the distance from anthropogenic sources increases. While these natural processes reduce immediate concentrations, managing the production and consumption of ibuprofen remains the most effective long-term strategy for pollution control.

In wastewater systems, both the influent and the effluent represent significant reservoirs of ibuprofen due to their direct connection to human consumption and excretion. The concentration of ibuprofen in influent wastewaters from the wastewater treatment plant in Ostrava, Czech Republic, ranged from 9511 to 94 054 ng L^{-1},[46] in Ebro Delta, Spain, from 11 000 to 17 452 ng L^{-1},[28] and in Vhembe and Mopane Districts, South Africa, from below limit-of-detection to 114 000 ng L^{-1}.[44] The outcomes exhibited high ibuprofen concentrations, caused by the untreated sewage inputs rich in pharmaceutical residues. In post-treatment, effluent wastewaters showed reduced levels of ibuprofen, such as in Ostrava (78–1597 ng L^{-1}) and Ebro Delta (below limit-of-detection to 15 864 ng L^{-1}), indicating partial removal through treatment processes. However, the presence of ibuprofen in effluents was still considerable, *e.g.*, up to 60 000 ng L^{-1} in South Africa (Table 1). This challenge calls for more efficiencies in current wastewater treatment technologies for pharmaceutical removal.

2.2. Effect

Table 2 shows the biological effects of ibuprofen on various species. In plants, ibuprofen exposure induces oxidative stress, impairs photosynthetic processes, inhibits seed germination, and reduces antioxidant enzyme activity and root elongation. In animals, excessive concentrations lead to disrupted hormonal secretion, increased apoptotic activity, and reduced cell viability; it also correlates with lower white blood cell counts, weight loss, and decreased cocoon production. In humans, ibuprofen exposure is associated with inhibited angiogenesis, reduced hormone ratios, which can lead to compensated hypogonadism. Moreover, ibuprofen exposure decreases gonocyte numbers in fetal gonads, and suppress secretion of essential growth factors and cytokines. The findings demonstrate the widespread ecological and physiological impact of ibuprofen on a range of disparate taxa.

In plants, ibuprofen exerts phytotoxicity on physiological activities. From Table 2, it can be observed that exposure to ibuprofen at a concentration as low as 0.25 μg L^{-1} induced oxidative stress in the seagrass *Cymodocea nodosa*; and at high concentrations of 25 μg L^{-1}, photosynthesis activity and antioxidant enzyme activity were suppressed.[49] The total content of chlorophyll increased from 0.75 to 1.25 mg per g fresh weight. The author assumed that greater quantities of chlorophyll compared to normal state could increase the probability of photoinhibition. Similarly, in *Lactuca sativa* seeds, a concentration of 3 ng per g soil resulted in a 50% reduction in root elongation,[53] and in *Vigna unguiculata*, the concentration of ibuprofen at 10 000 ng g^{-1} caused 50% inhibition of seed germination after 50 days.[54] These works suggested that ibuprofen threatened plant growth and development by interfering with cellular homeostasis and reproductive success. Consequently, the presence of ibuprofen in soil and water systems can pose a potential endangerment to plant populations and ecosystem stability.

In animals, ibuprofen also exerted several adverse effects, *e.g.*, impacting survival, reproduction, and immune function. Table 2 indicates that in the fish *Acanthopagrus arabicus*, exposure to 1 μg mL^{-1} reduces cell viability by 60% and disrupts estrogen synthesis and reproduction through altered 11-ketotestosterone secretion.[59] In the fish *Rhamdia quelen*, concentrations of 0.1 to 1.0 μg L^{-1} decreased white blood cell counts in the range from 29% to 98% for each type of cell.[60] Meanwhile, in earthworms, 100 μg L^{-1} of ibuprofen could reduce the body weight by 30% and cocoon production by 40% after 28 days.[58] Besides, in the river mussel *Unio tumidus*, 0.8 μg L^{-1} increased apoptotic activity and inhibited metabolic balance in the digestive gland.[56] The toxicity of ibuprofen in some species mentioned above spans a variety of physiological systems; therefore, ibuprofen pollution has the potential to initiate population decline and ecological disruptions in contaminated environments.

In humans, exposure to varied ibuprofen levels is linked to significant physiological disruptions, such as in reproductive and cellular functions. From the investigation in first-trimester human fetal testes and ovaries under ibuprofen exposure, it was found that ibuprofen reduces gonocyte numbers by 22% and 49%, respectively, indicating reproductive and hormonal dysfunction.[65] In adult males, ibuprofen concentrations of 25 to 100 μg mL^{-1} in plasma decreased the testosterone-to-luteinizing hormone ratio.[66] This impact in the long term led to the compensated hypogonadism. Furthermore, at 1000 μM, ibuprofen inhibited angiogenesis in human umbilical vein endothelial cells by reducing tube formation, migration, and proliferation.[64] Seriously, in bone marrow-derived mesenchymal stromal cells, ibuprofen at 25 μg L^{-1} strongly suppressed the secretion of critical factors, including monocyte chemoattractant protein 1, hepatocyte growth factor, interleukin (IL)-6, and vascular endothelial growth factor, from 20% to 44%.[63] The significant decrease can disrupt hematopoiesis, increasing the risk of anemia, and weaken immune responses in the physiological system in humans. Raising concerns about the long-term implications of ibuprofen contamination for human health in both clinical and environmental contexts should be paid intensive attention to prevent those negative effects.

3. Synthesis of adsorbents

3.1. Activated carbons derived from bio-wastes

3.1.1. H_3PO_4-AC. The H_3PO_4 activation of biomass-derived activated carbons involves a multi-step process that enhances the porosity and surface functionality. The treatment of H_3PO_4 initially induces the depolymerization of cellulose and the dehydration of biopolymers, which form aromatic structures, and the elimination of phosphate clusters subsequently.[67,68] Acid hydrolysis process is induced by the diffusion of H_3PO_4 molecules into the precursor biochar, facilitating extensive pore formation.[69] Besides, phosphoric acid reacts with organic species in the biomass to form phosphate and polyphosphate groups that induce a dilation process and generate an accessible porous structure.[69] Carbon under calcination at high temperatures also reacts with phosphorus oxides (P_2O_5) to further enhance pore formation.[67] Activated carbon generated is chemically and thermally highly stable according to the presence of C–O–P functional groups, which also facilitate its surface acidity.

Table 3 shows that there is no obvious correlation between the two variables: the calcination temperature and the surface area of activated carbon. However, several studies suggested an inverse relationship. For example, a past study reported that H_3PO_4-activated *Populus tremula* carbon showed a decrease in surface area from 1381 m^2 g^{-1} to 910 m^2 g^{-1} when the calcination temperature increased from 400 °C to 700 °C.[70] A similar trend was observed in the study by Liang *et al.*[71] Indeed, these authors conducted the synthesis of willow wood-derived activated carbons using H_3PO_4, where the surface area declined from 992 m^2 g^{-1} at 350 °C to 608 m^2 g^{-1} at 550 °C. This reduction in surface area at higher temperatures is likely due to excessive carbonization and structural collapse. Other contributing factors include pore shrinkage and the loss of surface functional groups through volatilization.

Based on SEM analysis, the effect of carbonization temperature on morphology was also indicated (Fig. S2). As the

Table 2 Effect of ibuprofen on organisms

Species	Concentrations and main effects	Ref.
Seagrass *Cymodocea nodosa*	At 0.25 and 2.5 μg L^{-1}: oxidative stress At 25 μg L^{-1}: reduced antioxidant enzyme activity, metabolites production, impaired photosynthetic function	49
Vigna unguiculata	IC_{50} at 1253 mg g^{-1}	50
Oryza sativa L.	Ibuprofen-caffeine at 500/5000 μg L^{-1} increased the yield of rice up to 51%	51
Lemna gibba L.	At 1 mg L^{-1} and after 8 days, the number of leaves increased (+12%) and multiplication rate (MR, a growth rate measures how the frond number increases over a specific time) increased (+10%)	52
Lactuca sativa seeds	At 3 ng per g soil: root elongation showed 50% of the reduction	53
Vigna unguiculata L. Walp	At 10 000 ng g^{-1}, 50% of inhibition in seed germination after 50 days	54
Chlorella sorokiniana	- Concentration from 0–100 μg L^{-1} after 4 days, cell density decreased from 81 to 30 × 10^4 cells per mL	55
Unio tumidus	At 0.8 μg L^{-1}, after 14 days - NAD^+/NADH ratio in the digestive gland decreased from 4 to 0.5 μmol g^{-1} - Apoptotic activities in the digestive gland increased. Cathepsin D activity increased from 1 nmol min^{-1} mg^{-1} to 4 nmol min^{-1} mg^{-1}	56
Chironomus riparius	- LC_{10} 48 h = 0.024 μg L^{-1}	57
Earthworms	At 100 μg L^{-1}, the weight of earthworm decreased 30% after 14 days and the cocoon number decreased 40% after 28 days	58
Acanthopagrus arabicus	Estrogen synthesis and reproduction were negatively affected *via* the decrease in secretion of 11-KT at testicular and increase in secretion of 11-KT at ovarian - At 1 μg mL^{-1}, cell viability decreased by 60%	59
Rhamdia quelen	- At 0.1 to 1.0 μg L^{-1}, the white blood cell count decreased, *e.g.*, neutrophils, lymphocytes, monocytes and thrombocytes count reduced from 29% to 98% - At 10 μg L^{-1}, the increase in glutathione peroxidase activity	60
Cyprinus carpio	- At 2000 μg kg^{-1}, lymphocytes decreased by 34% - At 2000 μg kg^{-1}, the transcriptomic profile, *e.g.*, *cyp1a*, *thrα*, *thrβ*, and *sod*, showed decrease	8
Rana catesbeiana tadpoles	- LC_{50} at 42 mg L^{-1} - At 14 μg L^{-1}, 26 mRNA transcripts changed in the liver of exposed tadpoles within 6 days	61
Human face	Ibuprofen dose was associated with decreased blood oxygen level-dependent in the during emotional face processing	62
Human bone marrow-derived mesenchymal stromal cells	- At 25 μg L^{-1}, the secretion of prostaglandin E2 substantially reduced - At 25 μg L^{-1}, for 3 days, the secretion of monocyte chemoattractant protein 1, hepatocyte growth factor, interleukin (IL)-6, and vascular endothelial growth factor strongly decreased from 20% to 44%	63
Human umbilical vein endothelial cells	At 1000 μM, angiogenesis in human umbilical cord vein endothelial cells was inhibited through the decrease in tube formation, migration and cell proliferation up to 1.9 times and inhibition of the cell cycle S-phase and promotion of apoptosis	64

Table 2 (*Contd.*)

Species	Concentrations and main effects	Ref.
First-trimester human fetal testes/ovaries	Number of gonocytes was decreased in first-trimester human fetal testes exposed *in vitro* to ibuprofen (−22%) and also in ovaries exposed to ibuprofen (−49%)	65
Hormones in adult males	Ibuprofen in plasma ranged on average from 25 to 100 μg mL^{-1}, which caused compensated hypogonadism and decreased the ratio of testosterone to luteinizing hormone	66

calcination temperatures were increased, the surface became increasingly rough with more defects, and cavities became bigger, which corresponded to changes in the structure.[71] The formation of bigger pores suggested pore coalescence, which could lower the porosity. Carbonization at very high temperatures could lead to the collapse of pore walls, leading to the loss of microporosity. It is explained that the pore collapse decreases the microstructured channel, diminishing the surface area of activated carbons. As a result, morphological alterations result in a decrease of surface area, which is critical for adsorption.

As activation by H_3PO_4 is ineffective to improve the surface area, secondary activation or two-stage activation may be required. For example, Osman *et al.* used KOH to re-activate H_3PO_4-activated carbons from brewer's spent grain waste.[102] These authors reported an increase in BET surface area from 497 $m^2\ g^{-1}$ (first activation with H_3PO_4) to 692 $m^2\ g^{-1}$ (re-activation with KOH). The improvement was attributed to the development of new pores through chemical reactions between the carbon matrix and KOH. As a result, the morphological alterations were also observed. However, secondary activation is a high-cost and time-consuming additional stage, and should be considered.

3.1.2. $ZnCl_2$-AC. $ZnCl_2$ plays a critical role in the activation of biochars to facilitate both physical and chemical transformation. First, as an effective dehydrating agent, $ZnCl_2$ breaks glycosidic, hydroxyl, and carbonyl linkages to produce zinc chloride hydrates and catalyzes cellulose and hemicellulose decomposition.[80] This accelerates the depolymerization of cellulose, where $ZnCl_2$, as a Lewis acid, coordinates oxygen atoms of glycosidic bonds to cleave them.[103,104] Moreover, $ZnCl_2$ acts as a catalyst in decarboxylation reactions and aromatization for forming aromatic structures.[80] Reduction reactions of ZnO with carbon also release Zn vapor and CO_2/CO gases, generating pores in activated carbon.[105] As a result, activation improves the structure of carbon by adding certain types of benzene-ring networks, significantly improving the porosity and surface chemistry.

The significant effects of $ZnCl_2$ on biochar activation were evaluated by comparing the surface chemistry of biochars and $ZnCl_2$-activated carbons (Fig. S3).[106] Through *in situ* DRIFTS analysis, it was found that at 300 °C, pine needle-derived biochars showed characteristic peaks at 3500 to 1200 cm^{-1}. However, the absence of an absorption peak for =C–H and the presence of the –C–H bond indicate that dehydrogenation occurs at minimal levels. In contrast, $ZnCl_2$-impregnated pine needle treated under the same conditions demonstrated enhanced dehydrogenation of alkanes (–C–H) to alkenes (=C–H). Additionally, the authors observed that at high calcination temperatures (>500 °C), the disappearance of =C–H and olefinic C=C, along with the predominance of aromatic C=C, indicates increased aromatization. Unlike the heat treatment without $ZnCl_2$ impregnation $ZnCl_2$ suppressed the adsorption of CO_2 and acted as a catalyst for condensation and aromatization rather than cracking reactions.

The surface area of $ZnCl_2$-activated carbon is considerably reliant on biomass origin and calcination temperature.[84] In the case of activated carbons synthesized from forestry residue biomass, as the calcination temperature increased from 400 °C to 600 °C, the surface area consistently increased from 569 $m^2\ g^{-1}$ at 400 °C to 632 $m^2\ g^{-1}$ at 500 °C to 849 $m^2\ g^{-1}$ at 600 °C. This trend implies that the increase in temperature enhances pore development in activated carbon. However, the surface area of waste wood-based activated carbon had an opposite trend. Its surface area increased significantly from 852 $m^2\ g^{-1}$ to 1430 $m^2\ g^{-1}$ when the temperatures increased from 400 °C to 500 °C. However, the surface area decreased to 1219 $m^2\ g^{-1}$ with further heating to 600 °C. The outcome implied that over-carbonization or collapse of pores reduces porosity at higher temperatures. The surface area of forestry residue biomass-derived activated carbons is superior at elevated temperatures. Meanwhile, the surface area of waste wood-derived activated carbon was optimal at 500 °C, but the higher temperatures of carbonization decreased the surface area of activated carbon.

3.1.3. K_2CO_3-AC. The activation of biochars using K_2CO_3 significantly enhances the porosity and structural properties of activated carbons through a series of chemical reactions. At temperatures higher than 700 °C, K_2CO_3 undergoes reductive decomposition, producing potassium metal vapor that continuously erodes the carbon matrix, which enlarges and forms pores.[107] In a vapor environment, the intercalation of potassium into the carbon lattice boosts gasification and facilitates pore generation, while in a CO_2 environment, potassium catalyzes a deeper pore structure and enhances the high graphitization.[107] The catalytic effect of K_2CO_3 increases the carbon conversion rate as potassium species penetrate the carbon structure, expanding the aromatic layers, and distorting the framework, thereby improving the internal and external structures.[108] This catalytic reaction demonstrates that K_2CO_3 significantly

Table 3 Production of activated carbons derived from bio-wastes

Type of waste	Activator	Carbonization temperature (°C)	BET surface area ($m^2\ g^{-1}$)	Ref.
Castor seed hull	H_3PO_4	700	785.4	72
Bamboo biomass	H_3PO_4	500	1063	73
Bamboo biomass	H_3PO_4	500	1398	73
Bamboo biomass	H_3PO_4	500	1492	73
Grass biomass	H_3PO_4	700	756	74
Banana trunk	H_3PO_4	583	1290	75
Sunflower straw	H_3PO_4	600	794	76
Willow branch wastes	H_3PO_4	550	608	71
Willow branch wastes	H_3PO_4	350	992	71
Corn stigmata	H_3PO_4	400	598	77
Populus tremula	H_3PO_4	400	1381	70
Populus tremula	H_3PO_4	550	1120	70
Populus tremula	H_3PO_4	700	910	70
Acacia mangium	H_3PO_4	900	1767	78
Cellulose	H_3PO_4	200	433	79
Cellulose	H_3PO_4	250	621	79
Cellulose	H_3PO_4	300	1096	79
Cellulose	H_3PO_4	400	1019	79
Cellulose	H_3PO_4	500	988	79
Cellulose	H_3PO_4	600	868	79
Cellulose	H_3PO_4	700	677	79
Bamboo fibers	$ZnCl_2$	600	2129	80
Bamboo powder	$ZnCl_2$	600	1854	80
Parenchyma cells	$ZnCl_2$	600	1724	80
Coal slime	$ZnCl_2$	500	657	81
Deashing coal slime	$ZnCl_2$	500	918	81
Lotus root	$ZnCl_2$	550	1560	82
Cotton fiber	$ZnCl_2$	550	1148	82
Willow branch	$ZnCl_2$	350	983	71
Willow branch	$ZnCl_2$	550	1635	71
Sugarcane bagasse	$ZnCl_2$	900	1387	83
Rice husk	$ZnCl_2$	600	750	83
Forestry residue biomass	$ZnCl_2$	400	569	84
Forestry residue biomass	$ZnCl_2$	500	632	84
Forestry residue biomass	$ZnCl_2$	600	849	84
Waste wood	$ZnCl_2$	400	852	84
Waste wood	$ZnCl_2$	500	1430	84
Waste wood	$ZnCl_2$	600	1219	84
Corn stigmata fibers	$ZnCl_2$	400	389	77
Weeping willow	$ZnCl_2$	550	1980	85
Moso bamboo	K_2CO_3	800	1802	86
Peanut shells	K_2CO_3	800	1150	87
Bamboo shoot shells	K_2CO_3	600	1084	88
Bamboo shoot shells	K_2CO_3	700	1429	88
Bamboo shoot shells	K_2CO_3	800	1440	88
Quercus variabilis cork	K_2CO_3	600	366	89
Quercus variabilis cork	K_2CO_3	700	1981	89
Quercus variabilis cork	K_2CO_3	800	2215	89
Quercus variabilis cork	K_2CO_3	900	2051	89
Bamboo shoot shell	K_2CO_3	600	748	90
Bamboo shoot shell	K_2CO_3	700	1323	90
Bamboo shoot shell	K_2CO_3	800	1986	90
Corncob powder	K_2CO_3	800	1896	91
Black cumin residues	K_2CO_3	900	2211	92
Petroleum coke	K_2CO_3	700	601	93
Banana peels	$NaNH_2$	900	1170	94
Biogas residue	$NaNH_2$	800	1145	95
Waste tobacco stem	$NaNH_2$	550	2185	96
Hazelnut shells	$NaNH_2$	500	1833	97
Hazelnut shells	$NaNH_2$	550	2185	97
Hazelnut shells	$NaNH_2$	600	2321	97
Corncob	Pyroligneous acid	850	384	98

Table 3 (*Contd.*)

Type of waste	Activator	Carbonization temperature (°C)	BET surface area ($m^2\ g^{-1}$)	Ref.
Local date seed	H_2SO_4	900	577	99
Corn straws	$NaHCO_3$	800	1230	100
Pistachio shell	$Na_2S_2O_3$	800	775	101

enhances the reactivity and structural growth of biochars during activation.

The impregnation ratio of K_2CO_3 to biochar significantly influences the surface area and structural properties of activated carbon. The surface area is improved by increasing the K_2CO_3/biochar ratio *via* the catalytic action of potassium species, enhancing carbon gasification and pore formation. For instance, peanut shell-derived activated carbons show an increase in surface area from 502 $m^2\ g^{-1}$ to 1150 $m^2\ g^{-1}$ with the increase in K_2CO_3/biochar ratios from 0 to 2.[87] Similarly, Moso bamboo powder-derived carbon activated with K_2CO_3 at activator-to-feedstock ratios of 0 to 6 (by mass) displayed a growth in the surface area from 700 $m^2\ g^{-1}$ to 1802 $m^2\ g^{-1}$.[86] This trend can be attributed to the enhanced intercalation of potassium into the carbon matrix. The activity of potassium disrupts layers and enlarges pore structures (micropore volume increased from 0.27 to 0.78 $cm^3\ g^{-1}$ for the Moso bamboo powder-derived activated carbon,[86] and from 0.21 to 0.64 for the peanut shell-derived activated carbon).[87] However, excessive loading of potassium carbonate beyond an optimum ratio leads to structural degradation, over-gasification, and reduction in the yield of activated carbon. For example, the increased proportion of potassium carbonate has been associated with the reduction in the yield of activated carbon derived from peanut shells from 22% to 16% by weight.[86] Therefore, the potassium carbonate impregnation ratio must be regulated with great precision in order to achieve optimum porosity and surface area in the production of activated carbons.

3.2. Magnetic nanoparticles loaded on activated carbons derived from bio-wastes

The synthesis of magnetic activated carbon derived from biowaste involves a series of physicochemical treatments (Fig. 2). The raw biowaste is pretreated, dried and then calcined to eliminate moisture. This is followed by activation and pyrolysis in an oxygen-free atmosphere to yield activated carbons. Magnetic function is introduced by loading magnetic elements, by mixing activated carbons either with magnetic precursors (*in situ*) or with pre-formed magnetic particles (*ex situ*). The final magnetic activated carbon product is obtained after thorough washing and drying to produce a material that finds application in adsorption, separation, and catalysis.

3.2.1. $NiFe_2O_4$/AC. The synthesis of $NiFe_2O_4$ on activated carbon has two primary methods, *i.e.*, co-precipitation and hydrothermal synthesis, which differ in terms of synthesis time, temperature, and chemical reagents (Table 4). In the case of the co-precipitation method, Moussa *et al.* prepared $NiFe_2O_4$/corncob-derived activated carbons by mixing the as-prepared activated carbons, $FeCl_3$ and $NiCl_2$, followed by the addition of NH_4OH to adjust the pH to 11, which led to precipitation at room temperature within 30 min.[109] In a modified approach, Hemalatha *et al.* conducted a precipitation-assisted hydrothermal pathway, wherein the precipitate derived from NaOH-induced pH adjustment was subjected to hydrothermal treatment at 160 °C for 12 h and then calcined at 400 °C for 5 h.[110] The author demonstrated the uniform dispersion of $NiFe_2O_4$ in the range of 30–40 nm over *Peltophorum pterocarpum* seed-derived activated carbons, and they found out that $NiFe_2O_4$/AC had a high degree of crystallinity. Similarly, Nguyen *et al.* synthesized $NiFe_2O_4$/AC *via* a hydrothermal process by adding the AC derived from *Bidens pilosa* biomass in ethylene glycol with $FeCl_3$ and $NiCl_2$ and adding CH_3COONa and polyethylene glycol and then heating the suspension in an autoclave at 136 °C for 17 h.[111] Co-precipitation is the fastest synthesis method but requires precise pH control. In contrast, hydrothermal processing ensures a more uniform distribution of components, such as nickel ferrite. However, the process is much slower because of the extended heating and crystallization steps. The precipitation-assisted hydrothermal process achieves a balance between the reaction time and the material quality.

The effect of $NiFe_2O_4$ loading on surface area varied significantly depending on synthesis conditions and material interactions. According to the solvothermal method of synthesis of $NiFe_2O_4$/AC, the composite exhibited a surface area of 994 $m^2\ g^{-1}$, significantly surpassing $NiFe_2O_4$ (17.0 $m^2\ g^{-1}$) and *Bidens alba*-derived AC (450 $m^2\ g^{-1}$).[111] The solvothermal method facilitated homogeneous dispersal of the $NiFe_2O_4$ nanoparticles within the AC network in the absence of particle aggregation and the conservation of open porous texture. In contrast, AC/$NiFe_2O_4$ synthesized by a precipitation method had a surface area (153 $m^2\ g^{-1}$) lower than that of corncob-derived AC (176 $m^2\ g^{-1}$) but higher than that of $NiFe_2O_4$ (90 $m^2\ g^{-1}$).[109] The precipitation process most likely resulted in the formation of larger $NiFe_2O_4$ clusters on the AC surface, partially blocking the inherent porosity and reducing the accessible surface area of AC. These results highlight how synthesis conditions affect the structural properties of the composite. Controlled solvothermal incorporation can enhance surface area, whereas uncontrolled deposition during precipitation leads to pore clogging. Therefore, optimizing the synthesis process is essential to ensure maximum surface area and functionality in $NiFe_2O_4$/AC composites.

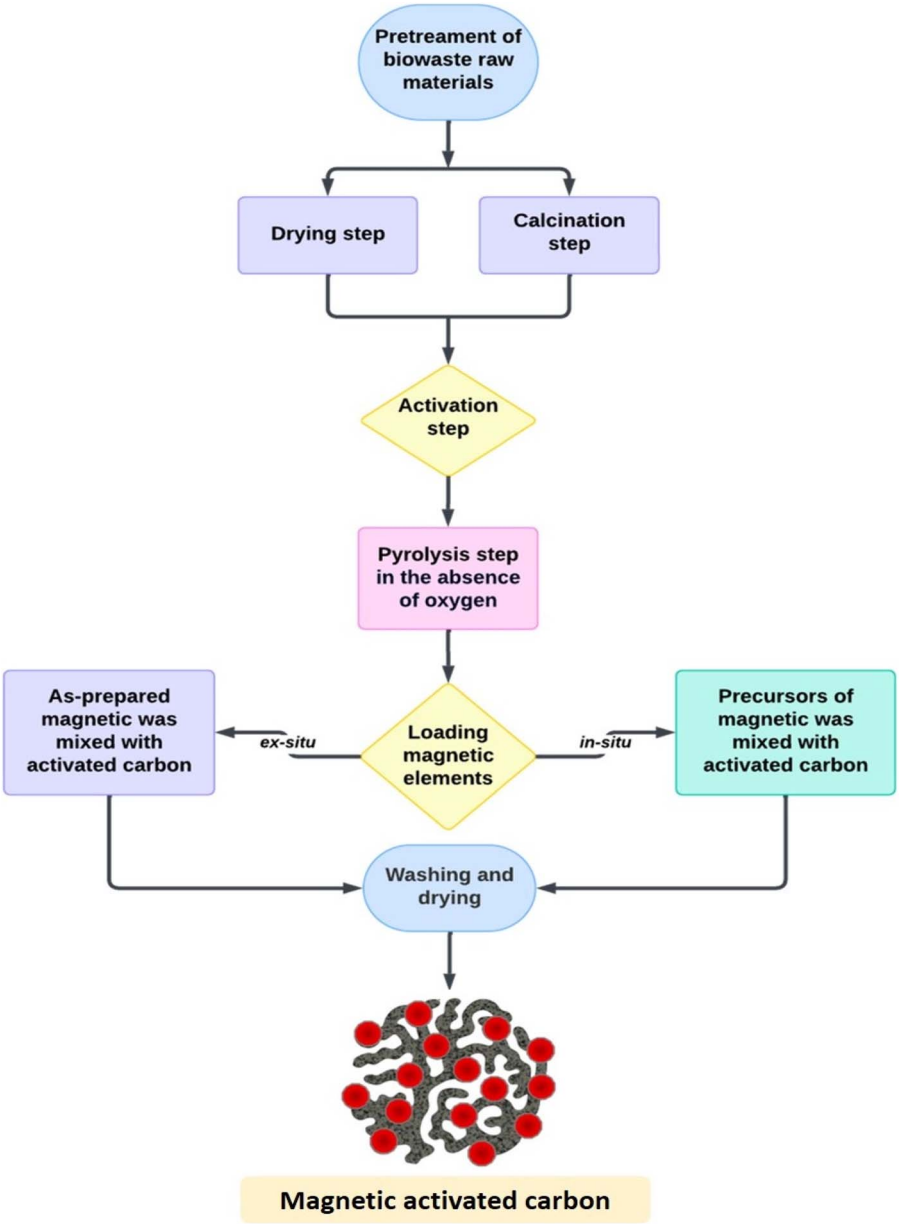

Fig. 2 Synthesis procedure of magnetic activated carbon.

The saturation magnetization of $NiFe_2O_4$/AC composites is typically lower than that of pure $NiFe_2O_4$ due to the presence of non-magnetic activated carbon (AC), which has the tendency to reduce the overall magnetic response. Hazelnut shell-activated carbon/$NiFe_2O_4$ has a saturation magnetization of 16.2 emu g^{-1}, whereas that of $NiFe_2O_4$ nanoparticles ranged from 28 to 37 emu g^{-1}.[112] These findings agree with other reports on $NiFe_2O_4$ nanoparticles synthesized by similar chemical methods, with saturation magnetization values ranging between 25 and 35 emu g^{-1}.[125] This indicates that the incorporation of AC into the composite has a great effect on its magnetic properties through declining magnetization.

3.2.2. $CoFe_2O_4$/AC. The fabrication of $CoFe_2O_4$/activated carbon composites involves various processes, *i.e.*, precipitation, hydrothermal, and single-step refluxing techniques (Table 4). The selection of a suitable synthesis technique is crucial. There are several parameters, *e.g.*, temperature, reaction time, and precursor composition, which significantly affect the surface area, porosity, and magnetic value in the resultant composite. For example, the synthesis temperatures ranged from 80 °C to 300 °C, synthesis times ranged from 2 h to 24 h, and various chemicals, *i.e.*, NaOH and methylbenzene were used.

The hydrothermal synthesis of $CoFe_2O_4$/activated carbon ensures precise control over the nanoparticle size and crystallinity in a pressurized environment.[120] First, $Fe(NO_3)_3$ and $Co(NO_3)_2$ were dissolved in ultrapure water along with bamboo leaf-derived activated carbons. Then, the pH was adjusted using

Table 4 Production of magnetic activated carbons derived from bio-wastes

Type of waste	Composite	Synthesis procedures	BET surface area ($m^2\ g^{-1}$)	Ref.
Seed pods of *Peltophorum pterocarpum*	$NiFe_2O_4$/AC	$NiFe_2O_4$ precursor was mixed with AC and calcined at 400 °C for 5 h	176	110
Bidens pilosa	$NiFe_2O_4$/AC	AC was dispersed in ethylene glycol, then Fe(III) and Ni(II) precursors were added under ultrasonication. The mixture was heated in a Teflon-lined autoclave at 136 °C for 17 h	994	111
Corncobs	$NiFe_2O_4$/AC	Fe(III) and Ni(II) precursors were mixed with the as-prepared AC. Then NH_4OH solution (25%) was added and stirred at room temperature. The precipitate of $NiFe_2O_4$ was formed on AC	332	109
Hazelnut shells	$NiFe_2O_4$/AC	AC was mixed with a solution containing Fe(III) and Ni(II) precursors. Then resulting mixture was then combined with poly vinyl pyrrolidone and dispersed using an ultrasonic bath. The suspension was finally transferred in a Teflon-lined autoclave and maintained at 180 °C for 12 h	288	112
Commercial cellulose	$MnFe_2O_4$/AC	$MnFe_2O_4$ was added on AC surface *via* a simple one-pot solvothermal method. The mixture of solution precursor, AC, and ethylene glycol were mixed in ultrasound bath. Then the dispersed solution was added to sodium acetate and polyethylene glycol. The mixture was placed in Teflon-lined autoclave at 200 °C for 10 h	265	113
Durian shell	$MnFe_2O_4$/AC	The solutions of Fe(III) and Mn(II) salts were mixed with AC and stirred well. The solid was calcined at 600 °C for 4 h	519	114
Black cumin waste	$MnFe_2O_4$/AC	$MnFe_2O_4$/AC was synthesized *via* microwave-assisted co-precipitation by mixing AC with Fe(III) and Mn(II) salts under alkaline conditions (3 M NaOH). After stirring for 30 min, the dark brown precipitate was exposed to microwave radiation for 3 min	781	115

Table 4 (*Contd.*)

Type of waste	Composite	Synthesis procedures	BET surface area ($m^2\ g^{-1}$)	Ref.
Pyrolytic coke	$MnFe_2O_4$/AC	AC was stirred in deionized water for 30 min, then Fe(III) and Mn(II) precursors were added. A 5 M NaOH solution was added dropwise, and the mixture was stirred at 70–80 °C for 3 h. The precipitate was obtained and dried	61	116
Walnut wood	$CoFe_2O_4$/AC	Co(II) and Fe(III) precursors was prepared, followed by the addition of AC. The solution was heated to 80–90 °C, and 5 M NaOH was added. The AC/$CoFe_2O_4$ composite was magnetically separated, washed, and dried at 105 °C for 24 h	523	117
Eucommia ulmoides Oliver	$CoFe_2O_4$/AC	The suspended solution of AC and Fe(III) and Co(II) precursors were dispersed in deionized water under ultrasonic treatment. Then the mixture was treated with 0.008 mol NaOH and underwent a hydrothermal reaction at 180 °C for 12 h in a Teflon-lined autoclave	1227	118
Eucommia ulmoides Oliver	$CoFe_2O_4$/AC	Fe(III) and Co(II) precursors were dissolved in deionized water and treated with ultrasound for 15 min. 0.008 mol NaOH was added slowly, and the mixture was stirred. The precipitated was then dispersed in the mixture of AC and methylbenzene *via* ultrasonic treatment. As-prepared powder was calcined at 300 °C in 2 h	1208	118
Coconut shell	$CoFe_2O_4$/AC	The $CoFe_2O_4$/AC were synthesized using a single-step refluxing method. Firstly, AC was stirred in NaOH solution to form a suspension. The suspension was heated to 100 °C, and the solution containing Fe(III) and Co(II) precursors was then added. The mixture was refluxed at 100 °C in 2 h	760	119

Table 4 (*Contd.*)

Type of waste	Composite	Synthesis procedures	BET surface area ($m^2\ g^{-1}$)	Ref.
Bamboo leaves	$CoFe_2O_4$/AC	Fe(III) and Co(II) were dissolved in ultrapure water along with activated carbon. The pH was adjusted using 5 mol per L NaOH. The mixture was then heated at 200 °C for 24 h in a Teflon-lined stainless-steel autoclave. The resulting black precipitate was collected and thoroughly washed with ultrapure water and ethanol	237	120
Prosopis juliflora	Fe_3O_4/AC	Fe(II) and Fe(III) solutions were prepared and AC was added with stirring at 80 °C for 3 h. Ammonia solution was then added dropwise. The nanocomposite was recovered magnetically and washed with ethanol/distilled water mixture	632	121
Vine shoots	Fe_3O_4/AC	Aqueous solutions of 0.2 M Fe(III) and 0.1 M Fe(II) were stirred at 80 °C for 10 min. Activated carbon was then added and stirred for 30 min. Then, 3.4 M NaOH was added dropwise. The resulting black powder was filtered, washed, and dried at room temperature for 24 h	759	122
Banana peel	Fe_3O_4/AC	As-synthesized Fe_3O_4 were loaded onto AC using the immersion method. AC was mixed with a Fe_3O_4 nanoparticle solution for 3 h. The nanocomposite was then dried at 110 °C for 12 h	395	123
Tea waste	Fe_3O_4/AC	AC powder was added to a 30 mL solution of Fe(III) and Fe(II) at room temperature. The mixture was stirred for 1 h, followed by NH_4OH addition to form Fe_3O_4/AC nanocomposite	720	124

5 mol per L NaOH. The mixture was then heated at 200 °C for 24 h in a Teflon-lined stainless-steel autoclave. The presence of $CoFe_2O_4$ was confirmed by lattice spacings of 0.49, 0.25 and 0.15 nm corresponding to the (1 1 1), (3 1 1), and (4 4 0) facets of $CoFe_2O_4$. Moreover, the XRD patterns revealed the presence of $CoFe_2O_4$ nanoparticles, with characteristic peaks at 30°, 36°, and 63° for the spinel phase within the activated carbon matrix. These results showcased the efficacy and practical applicability of the hydrothermal process for the synthesis of high-performance adsorbents to clean up the environment.

The precipitation method provides a simple and effective way for the synthesis of $CoFe_2O_4$/activated carbon composites under alkaline conditions.[117] In this method, $CoCl_2$ and $FeCl_3$ precursors were synthesized, and then walnut wood-derived ACs were incorporated. The solution was heated to 80–90 °C, and 5 M NaOH was added. BET analysis revealed an increased specific surface area of 523.4 $m^2\ g^{-1}$ for $CoFe_2O_4$/activated carbon compared to 501 $m^2\ g^{-1}$ for the unmodified activated carbon. This increase may be attributed to the controlled precipitation of $CoFe_2O_4$, which prevents pore blockage and maximizes active site availability. Moreover, the saturation magnetization of $CoFe_2O_4$ was 98 emu g^{-1}, although it was lower in $CoFe_2O_4$/AC composite at 42 emu g^{-1}. These findings confirm that the precipitation method can effectively produce

magnetically responsive adsorbents with high surface area for applications in wastewater treatment.

The one-pot refluxing technique is a low-energy, scalable technique to synthesize $CoFe_2O_4$/activated carbon composites under mild conditions.[119] In this technique, coconut shell-derived AC was dispersed in 0.085 mol NaOH solution to form a suspension. The solution was heated to 100 °C, and $Fe(NO_3)_3$ and $Co(NO_3)_2$ precursor solutions were added. Then, the mixture was circulated at 100 °C within 2 h. The mild reaction conditions utilized in this process not only conserve energy but also guarantee structural stability for the activated carbon, which is a sustainable method for the large-scale production of adsorbents.

3.2.3. Fe_3O_4/AC. Table 4 indicates that precipitation is the most applied method for synthesizing Fe_3O_4/activated carbon composites due to the simplicity, cost-effectiveness, and scalability of the process. This process is obtained by mixing iron salts with activated carbons and introducing a base such as NaOH or NH_4OH in order to change the pH, which occur in reactions, *i.e.*, (1)–(3).

$$Fe_{(aq)}{}^{3+} + 6OH_{(aq)}{}^{-} \rightarrow 2Fe(OH)_{3(aq)} \quad (1)$$

$$Fe_{(aq)}{}^{2+} + 2OH_{(aq)}{}^{-} \rightarrow Fe(OH)_{2(aq)} \quad (2)$$

$$2Fe(OH)_{3(aq)} + Fe(OH)_{2(aq)} \rightarrow Fe_3O_{4(S)} + 4H_2O_{(aq)} \quad (3)$$

In the precipitation method, the alkaline media facilitate the formation of Fe_3O_4 nanoparticles on the carbon surface. In contrast, alternative synthesis methods, *e.g.*, hydrothermal, solvothermal, or calcination, are often more complex to implement, as they require high-pressure reactors, precise temperature control, or extended reaction times. These requirements can can increase both the complexity and the overall cost of production. Consequently, chemical precipitation is often preferred for its accessibility and simplicity. However, the precipitation method has remarkable limitations, such as the potential for uneven particle distribution on the activated carbon surface. Such non-uniformity may affect the purity of the composite and performance in sensitive applications. Besides, the challenge of removing residual ions, including Na^+ or $NH_4{}^+$ from the final product, needs to be considered.

The conventional immersion method is a utilized technique for synthesizing Fe_3O_4-loaded activated carbons. For example, activated carbons were derived from banana peel and salvia seed bio-sources.[123] The Fe_3O_4 nanoparticles were synthesized *via* a chemical co-precipitation method using Fe^{2+} and Fe^{3+} salts in an alkaline medium, followed by ultrasonication. The activated carbon was then immersed in a Fe_3O_4 nanoparticle suspension, stirred vigorously for 3 h, and subsequently dried to obtain the Fe_3O_4/activated carbon composite. Characterization techniques including SEM confirmed the large pores and rough surface of both hybrids with many clusters of magnetite. Brunauer–Emmett–Teller analysis showed the very low surface area of banana peel and salvia seed-derived activated carbon/Fe_3O_4. Meanwhile, the surface area of banana peel-derived activated carbon, in several reports, was so far higher, ranging from 295 $m^2\ g^{-1}$ to 1928 $m^2\ g^{-1}$.[126–128] Compared to other methods, such as hydrothermal synthesis or *in situ* precipitation, the immersion method is more sustainable and energy-efficient, as it operates without the intensive heating required by other approaches.

3.2.4. $MnFe_2O_4$/AC. Table 4 demonstrates that there were two primary methods for the synthesis of $MnFe_2O_4$/AC: calcination and precipitation. In the first approach, the loading of $MnFe_2O_4$ on durian husk waste-derived activated carbons was conducted through calcination at 600 °C for 2 h. Before this step, the mixture of $MnCl_2$, $Fe(NO_3)_3$, and as-prepared activated carbon was stirred well in 10 mL deionized water and dried. After heating, $MnCl_2$ and $Fe(NO_3)_3$ were dehydrated and decomposed, leading to the formation of intermediate oxides such as $Fe_yMn_{1-y}O$ and $Mn_xFe_{3-x}O_4$ with $0 \leq x, y \leq 1$.[129] Then, the nucleation and growth of the spinel phase of $MnFe_2O_4$ occurred. The activated carbon served as a structural support to anchor and provide functional groups that may facilitate nucleation and enhance the uniform dispersion of $MnFe_2O_4$ nanoparticles.[130] However, the optimization of calcination parameters should be careful, as prolonged exposure to elevated temperatures can degrade the activated carbon, diminishing its porosity and adsorption capacity.

For comparison, a $MnFe_2O_4$/cellulose-activated carbon composite was synthesized *via* a solvothermal method to ensure uniform $MnFe_2O_4$ particle deposition on the surface of the activated carbon.[113] The procedure was conducted by dispersing cellulose-based activated carbon in ethylene glycol, to which $FeCl_3$ and $MnCl_3$ were added. Sodium acetate and polyethylene glycol were added as stabilizers, and solvothermal treatment was done at 200 °C for 10 h. XRD and SEM characterization confirmed the formation of $MnFe_2O_4$ particles (100–300 nm) with homogeneous dispersion onto cellulose-activated carbon. The hybrid possessed a specific surface area of 265 $m^2\ g^{-1}$, lower than that of cellulose-activated carbon (912 $m^2\ g^{-1}$), due to partial pore blockage by $MnFe_2O_4$ particles. Magnetic measurements indicated that the composite had a saturation magnetization of 18 emu g^{-1}, less than that of pure $MnFe_2O_4$ (20 emu g^{-1}) due to the presence of non-magnetic cellulose-activated carbon.

Currently, to avoid the uneven deposition of precipitation method, Teymur and Güzel synthesized $MnFe_2O_4$/black cumin solid waste-derived activated carbons using a microwave-assisted chemical co-precipitation method.[115] In this approach, activated carbon was dispersed in deionized water, and $FeCl_3$ and $MnCl_2$ were added under alkaline conditions (pH ~10) using 3 M NaOH. The suspension was then shaken for 30 min and then irradiated with a microwave for 3 min to cause rapid nucleation and nanoparticle formation. The microwave-assisted route has lesser synthesis time demands than the solvothermal, hydrothermal, or calcination method because this method reduces reaction time to 3 min. XRD characterization of typical peaks testified to the existence of a spinel $MnFe_2O_4$ structure having dispersed nanoparticles on the carbon matrix. The hybrid composite had a specific surface area of 781 $m^2\ g^{-1}$, which was lower than that of activated carbon (2211 $m^2\ g^{-1}$).

Table 5 Kinetics of ibuprofen adsorption onto adsorbents derived from bio-wastes[a]

Bio-waste	Kinetic models	Best kinetic model	R^2	Ref.
Acacia sawdust	PFO, PSO	PFO	0.986	136
Tamarindus indica seeds	PFO, PSO	PSO	0.990	137
Helianthus annuus seed shell	PFO, PSO, ELO	PSO	0.990	138
Ginkgo biloba leaves	PFO, PSO	PSO	0.999	139
Avocado seeds	PFO, PSO	PSO	0.994–0.997	140
Sesame straw	PFO, PSO	PSO	0.990	141
Bamboo shoot shells of Moso bamboo	PFO, PSO	PSO	0.980	142
Sawdust materials	PFO, PSO, ELO, AVM	AVM	0.890–0.990	143
Waste bamboo	PFO, PSO	PSO	0.992	144
Red Mombin seeds	PFO, PSO	PSO	0.991	133
Corn cobs	PFO, PSO	PSO	0.996	133
Coffee husk	PFO, PSO	PSO	0.973	133
Ice cream bean seeds	PFO, PSO	PSO	0.968	133
Mango seed	PFO, PSO	PSO	0.996	133
Yeast milk	PFO, PSO	PSO	0.995	145
Orange peels	PFO, PSO	PSO	0.979	146
Cannabis sativa hemp	PFO, PSO	PSO	0.989	147
Schizolobium parahyba	PFO, PSO, ELO, general order	PSO, general order	0.990	148

[a] Note: pseudo first-order model: PFO, pseudo second-order model: PSO, Elovich model: ELO, Bangham model: BAN, and Avrami model: AVM.

Magnetic analysis revealed that the composite had a saturation magnetization value of 15 emu g^{-1}, much lower than that of $MnFe_2O_4$ (29 emu g^{-1}).

4. Adsorption of ibuprofen

4.1. Adsorption kinetics

The kinetics of adsorption of ibuprofen onto biomass-derived activated carbon is best described by the PSO model (Table 5), with R^2 values ranging from 0.968 to 0.999. The best fit with the PSO model suggests that the adsorption process follows chemisorption.[24,131] In this case, the main adsorption mechanism between the ibuprofen molecules and functional groups of carbon surface is chemical interaction.[132,133] Other works also indicated that the PSO model was best described on the adsorption of pharmaceutical products by activated carbons.[134,135] The high adsorption affinity of ibuprofen with biomass-derived activated carbon is attributed to its presence of oxygen-containing functional groups, high porosity, and large surface area, which favor strong interaction and enhance adsorption capacity. Furthermore, the high values of R^2 confirm that adsorption occurs at specific active sites. Surface chemistry and molecular interactions are, therefore, crucial. Activated carbon prepared from biowaste is a promising material for ibuprofen removal from water.

4.2. Adsorption isotherms

The adsorption of ibuprofen on activated carbons produced from biowaste was most described by the Langmuir model (Table 6), with excellent R^2 values of 0.978 to 0.999 and the maximum adsorption capacity (Q_{max}) reaching up to 491 mg g^{-1}. The excellent fit into the Langmuir model reveals that the adsorption process occurs on a homogenous monolayer of active sites of the same affinity for ibuprofen molecules.[149] In other research, Langmuir and Freundlich had been found to be the most utilized models, and the models greatly described the pharmaceutical adsorption on activated carbon.[150,151] This behavior confirms that biowaste-derived activated carbon possesses well-defined adsorption sites to enhance the interactions between ibuprofen and activated carbon. The high surface area and the presence of oxygen-containing functional groups of activated carbon can be the main reasons. Consequently, these findings confirm the advantages of biowaste-derived activated carbon as an efficient and sustainable adsorbent for pharmaceutical wastewater treatment.

4.3. Thermodynamics

Thermodynamic parameters describe the spontaneity and thermal nature of ibuprofen adsorption by activated carbon derived from biowaste (Table 7). The Gibbs free energy change ($\Delta G°$) indicated the spontaneity of adsorption, with highly negative values such as −68.65 kJ mol^{-1} for avocado seed-derived activated carbons and −52.81 kJ mol^{-1} for *Albizia lebbeck* seed pod-derived activated carbons.[154] This suggested a strongly spontaneous and favorable adsorption process, whereas less negative values, *i.e.*, 0.904 kJ mol^{-1} for sesame straw, expressed a less spontaneous interaction. The enthalpy change ($\Delta H°$) reflected the heat absorbed or released during adsorption, with positive values such as 58.62 kJ mol^{-1} for avocado seed-derived activated carbons[140] and 27.36 kJ mol^{-1} for the seed pod of *Erythrina speciosa*-derived activated carbons,[152] indicating an endothermic process. In contrast, the negative values, *i.e.*, −22.02 kJ mol^{-1} of sunflower seed shell-derived activated carbon, showed an exothermic reaction.[155] The entropy change ($\Delta S°$) is a measure of the disorder of the system; there are high positive values, which include 592 J mol^{-1} of avocado seed-derived activated carbons[140] and 540 J mol^{-1} for waste coffee-based activated carbons.[156] These results

Table 6 Isotherms of ibuprofen adsorption onto adsorbents derived from bio-wastes

Bio-waste	Isotherm models	Best isotherm model	R^2	Q_{max} (mg g^{-1})	Ref.
Acacia sawdust	Langmuir, Freundlich	Langmuir	0.979	122	136
Tamarindus indica seeds	Langmuir, Freundlich, Temkin	Langmuir	0.992	76	137
Helianthus annuus seed shells	Langmuir, Freundlich, Temkin	Langmuir	0.980	217	138
Ginkgo biloba leaves	Langmuir, Freundlich, Temkin, Dubinin–Radushkevich	Langmuir	0.995	178	139
Avocado seeds	Langmuir, Freundlich	Freundlich	0.995	38	140
Phyllostachys edulis	Langmuir, Freundlich	Langmuir	0.960	491	142
Sawdust residues	Langmuir, Freundlich, Sips, Redlich–Peterson, Temkin	Langmuir	0.986	211	143
Waste bamboo	Langmuir, Freundlich, Temkin, Dubinin–Radushkevich	Dubinin–Radushkevich	0.987	178	144
Red Mombin seeds	Langmuir, Freundlich	Freundlich	0.999	339	133
Yeast milk	Langmuir, Freundlich, Sips, Temkin, Dubinin–Radushkevich	Dubinin–Radushkevich	0.996	115	145
Erythrina speciosa pods	Langmuir, Freundlich, Dubinin–Radushkevich	Langmuir, Freundlich	0.996–0.999	98	152
Orange peels	Langmuir, Freundlich	Langmuir	0.978	70	146
Schizolobium parahyba	Langmuir, Freundlich, Dubinin–Radushkevich, Tóth	Tóth	0.990	447	148
Nauclea diderrichii	Langmuir, Freundlich	Langmuir, Freundlich	0.992	71	153

signified an increased randomness at the solid–liquid interface. Meanwhile, the negative value (−4.19 J mol^{-1}) for sesame straw-derived activated carbons indicated a decrease in disorder during adsorption.

4.4. Optimization by RSM

In response surface methodology (RSM)-based optimization of ibuprofen adsorption, two model designs are commonly employed: the central composite design (CCD) and the Box–Behnken design (BBD) (Fig. 3), both of which are used for the construction of second-order (quadratic) models of ibuprofen adsorption. Compared to BBD, CCD commonly involves a higher number of experimental runs, allowing for more detailed exploration of variable interactions.[162] The RSM procedure is initiated by the selection of key variables and responses. Second is experiment design, execution of experimental runs, and subsequent ANOVA analysis and model fitting. Next, optimal conditions are predicted and validated using confirmation tests. Variable analysis is performed by studying response surfaces, residual plots, and the relationship between predicted and actual values. This statistical technique in detail ensures model precision and determines the most important factors affecting the ibuprofen adsorption efficiency.

Table 8 presents the optimal conditions for ibuprofen adsorption using bio-waste-derived adsorbents, which are determined by RSM. For waste coffee-derived activated

Table 7 Thermodynamics of ibuprofen adsorption using adsorbents derived from bio-wastes

Adsorbents	$\Delta G°$ (kJ mol^{-1})	$\Delta H°$ (kJ mol^{-1})	$\Delta S°$ (J mol^{-1})	R^2	Ref.
Avocado seed-derived activated carbon	−68.65	58.62	592.2	—	140
Waste coffee-derived activated carbon	−4.81	153	540	—	156
Sunflower seed shell-derived activated carbon	−39.2	−22.02	57.7	0.990	155
Tamarindus indica seed-derived activated carbon	−4.08	−46.58	−0.147	0.992	137
Arachis hypogaea shell	−5.122	12.385	58.8	—	157
Fe_3O_4/Sawdust residue-derived activated carbon	−5.98	79.86	288	—	143
Sesame straw-derived activated carbon	0.904	10.93	−4.19	—	141
Tamarind seed-derived activated carbon	−8.57	−113.51	−0.363	0.963	158
Seed pods of *Erythrina speciosa*-derived activated carbon	−23.79	27.36	172	—	152
Waste coffee residue-derived activated carbon	−23.21	12.23	123.26	—	159
Nauclea diderrichii waste-derived activated carbon	−3.11	−30.32	91.29	—	153
Murumuru endocarp-derived activated carbon	−2.90	13.55	54.53	0.980	160
Coffee waste-derived activated carbon	−19.08	18.12	129.13	—	161
Albizia lebbeck seed pod-derived activated carbon	−52.81	−0.72	216.63	—	154

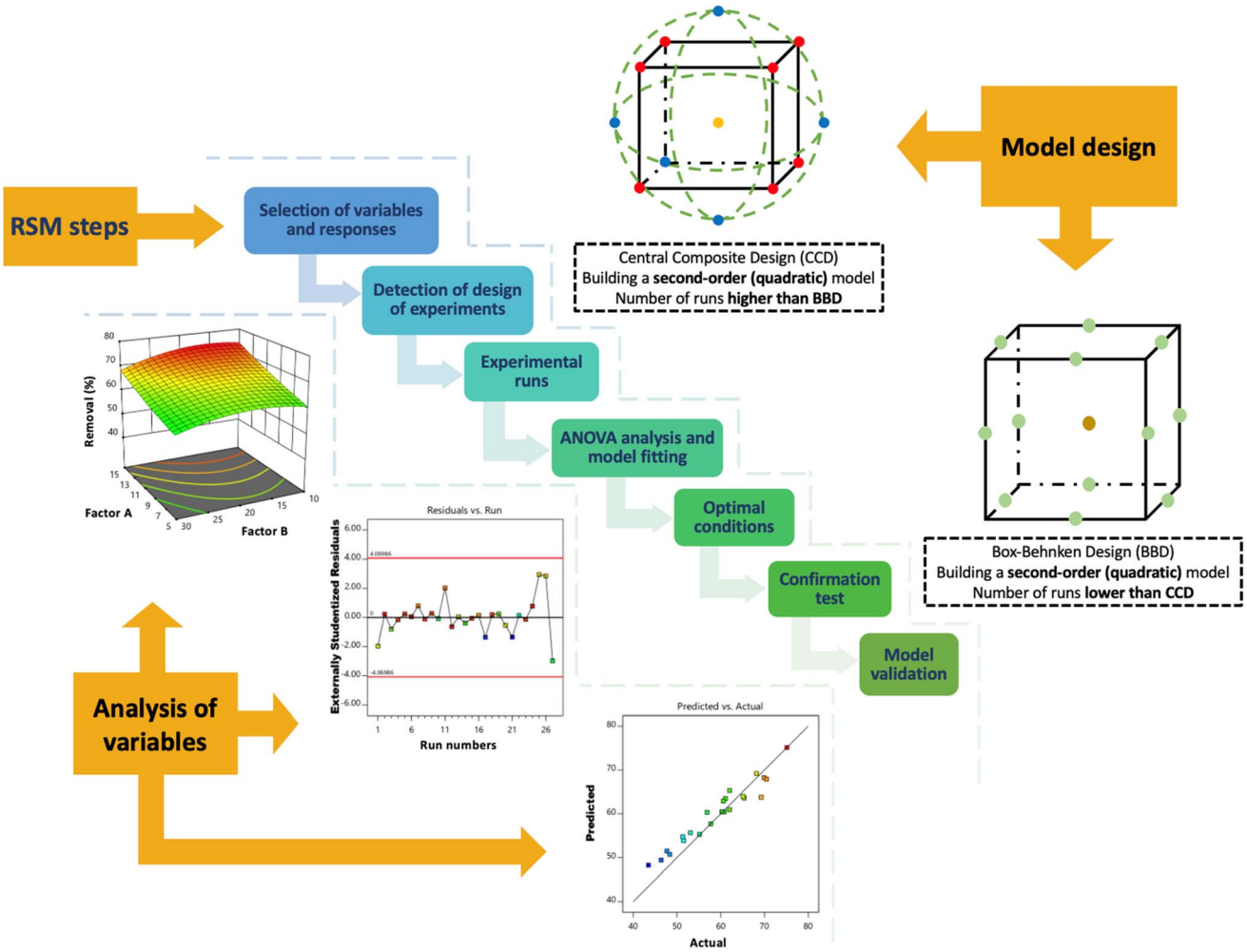

Fig. 3 Main steps in RSM optimization for the ibuprofen adsorption by activated carbon.

Table 8 Optimization of Ibuprofen adsorption by RSM using adsorbents derived from bio-wastes

Adsorbent	Model design	Variables and optimum condition	Predicted value (% or mg g^{-1})	Tested value (% or mg g^{-1})	Desirability	R^2	Ref.
Waste coffee-activated carbon	Box–Behnken design	- Temperature: 32 °C - Adsorbent weight: 0.1 g - pH: 6.8 - Time: 15 min	98%	100%	74–100%	0.94	156
Sunflower seed shells-activated carbon	Central composite design	- Adsorbent weight: 1 g L^{-1} - pH: 7 - Time: 60 min	—	100%	—	0.97	155
TiO_2/groundnut shell-activated carbon	Box–Behnken design	- Temperature: 30 °C - Adsorbent weight: 0.62 g L^{-1} - Time: 30 min	82%	79%	99%	0.99	157
Parthenium hysterophorus-derived activated carbon	Central composite design	- Adsorbent weight: 0.05 g - pH: 2 - Agitation speed: 160 rpm	100%	100%	—	0.98	163
Mung bean husk-derived activated biochar	Central composite design	- Adsorbent weight: 0.1 g L^{-1} - pH: 2 - Agitation speed: 200 rpm - Concentration: 20 mg L^{-1} - Time: 120 min	99%	99%	—	0.99	166

adsorbent, the optimal conditions are 32 °C, 0.1 g adsorbent weight, pH 6.8, and 15 min.[156] Meanwhile, another study showed that the optimal pH often ranges from 2 to 6.8, such as pH 2 for *Parthenium hysterophorus* and mung bean husk-derived activated adsorbents.[163] The pK_a of ibuprofen is approximately 4 to 5.[164] Below this value, the ibuprofen molecule charge is neutral state, but anionic if above this pK_a.[165] Notably, in two reports, the pH_{pzc} values of *Parthenium hysterophorus* and mung bean husk-derived activated adsorbents were 7.4 and 8.6, respectively. Therefore, the author confirmed that the electrostatic interaction was the main mechanism of adsorption.

A comparison between the tested and predicted values in Table 8 demonstrates the high precision of the RSM models. The majority of optimization reports were conducted using either central composite design or Box–Behnken design, with R^2 ranging from 0.94 to 0.99. For example, the predicted value for waste coffee-based activated carbon was 98%, and the tested value was 100% with desirability ranging from 74% to 100%.[156] Similarly, both sunflower seed shell- and *Parthenium hysterophorus*-derived activated carbons showed 100% adsorption efficiency of the test experiment.[163] Meanwhile, TiO_2/groundnut shell-derived activated carbons exhibited a slight discrepancy (predicted 82% and tested 79%).[157] Nevertheless, the desirability at 99% underscored a near-optimal condition. The high desirability scores, for instance, TiO_2/groundnut shell-(99%) and waste coffee-derived activated carbon (up to 100%), indicated that these conditions are not only theoretically optimal but also practically attainable.

4.5. Regeneration

The regeneration of bio-waste-derived activated adsorbents for ibuprofen desorption involves the use of various elution agents (Table 9), *e.g.*, NaOH, ethanol, methanol, HCl, ethylenediaminetetraacetic acid (EDTA), and acetonitrile. The higher affinity of these eluents with ibuprofen than that of the surface of biowaste-derived activated adsorbents is the main mechanism of desorption. Among these elution agents, NaOH is used in concentrations ranging from 0.1 M to 0.5 M. The increased alkaline properties of media lead to the deprotonation of adsorbed ibuprofen; therefore, the interactions, *i.e.*, hydrogen bonding, van der Waals forces, and π–π stacking, with the activated adsorbents are decreased. Ibuprofen molecules tend to increase the solubility in NaOH media, causing a desorption process. Similarly, organic solvents, including ethanol and methanol with concentrations from 0.1 M to 0.6 M can separate ibuprofen attached to the surface of activated adsorbent. The affinity of ethanol and methanol with ibuprofen was confirmed to be higher than that of ibuprofen with adsorbents.[167] Likewise, HCl can protonate the adsorbent surface to repel ibuprofen molecules.[168] Methanol is most widely applied as an elution agent due to its advantageous features, *e.g.*, the availability, and capacity of dissolving ibuprofen from adsorbents.

The reuse cycles of bio-waste-derived activated adsorbents from Table 9 are in the range of 4 to 10, with significantly different efficiencies between the first and final cycles. For example, *Ginkgo biloba* leaf-derived activated carbon possessed a very good efficiency, which decreased from 97% to 93% after 5 cycles.[139] Meanwhile, waste coffee residue-derived activated carbon declined sharply from 69% to 19% at the same number of cycles.[159] In another report, activated carbon derived from the seed pods of *Erythrina speciosa* maintained the adsorption efficiency for 7 cycles.[152] However, the efficiency significantly dropped from 50% at the 8th cycle to 5% at the 10th cycle. Reduced desorption efficiency with increasing cycles is attributed to the increasing saturation of active sites of the adsorbent and incomplete desorption of ibuprofen, leaving residual molecules that block subsequent adsorption. In addition, long-term exposure to elution agents can modify the surface chemistry or porosity of the adsorbents, thereby reducing the desorption process. These tendencies indicated trouble with regeneration efficiencies and the stability of long-term performance of biowaste-derived activated adsorbents.

The use of toxic elution agents, for instance, NaOH, methanol, and acetonitrile, in ibuprofen desorption poses environmental risks, which may lead to secondary pollution if not well managed. To mitigate these effects, strategies, *i.e.*, solvent recovery through distillation, neutralization of alkaline or acidic eluates, and the use of biodegradable solvents, can be employed to reduce the ecological impact.[174,175] Apart from the elution method, thermal treatment offers a promising alternative for regenerating activated adsorbents during post-adsorption of ibuprofen. This is because the thermal degradation of non-steroidal anti-inflammatory drugs commonly varied from 180 to 360 °C.[176–178] Thus, the thermal treatment method involves heating the spent adsorbent at controlled temperatures under an inert atmosphere to decompose and volatilize ibuprofen, thereby restoring active sites. Among the major advantages of thermal treatment is that partial degradation of ibuprofen molecules can enrich the surface chemistry of activated carbon with functional groups. Consequently, the affinity of adsorbents for ibuprofen in subsequent cycles was enhanced through improved π–π interactions or hydrogen bonding. The thermal treatment offers a simple regeneration process with less waste generation.

4.6. Adsorption mechanism

Table 10 outlines various adsorption mechanisms involved in the removal of ibuprofen using activated adsorbents derived from bio-wastes and supported with analytical techniques for verification of the interactions. The mechanisms identified are hydrogen bonding, π–π interactions, electrostatic interactions, pore-filling, hydrophobic interactions, cation–π interactions, and dipole–dipole interactions (Fig. 4). These mechanisms depend on some factors, such as the surface chemistry of the adsorbent, solution pH, and the physicochemical properties of ibuprofen (*e.g.*, pK_a ≈ 4.9). Analytical methods, *i.e.*, FTIR spectroscopy, XPS, and analysis of surface area were employed to provide evidence for the reported mechanisms.

For instance, hydrogen bonding was found as the main mechanism of ibuprofen adsorption onto waste coffee residue-derived activated carbon.[159] Indeed, XPS analysis revealed increased peak intensities of C=O carbonyls (28.27 eV of C 1s

Table 9 Regeneration of adsorbents derived from bio-wastes for the removal of ibuprofen

Adsorbent	Eluting solvent	Number of recycles	Adsorption (%, mg g^{-1}) at the first cycle	Adsorption (%, mg g^{-1}) at the final cycle	Ref.
Raphia hookeri kernel-derived activated carbon	0.1 M NaOH	5	96%	64%	169
Radix Angelica dahurica residue-derived activated carbon	Ethanol 95%	5	88%, equivalent to 10.9 mg g^{-1}	64%, equivalent to 8.8 mg g^{-1}	170
Sunflower seed shell-derived activated carbon	Acetonitrile 40%	4	89%	66%	155
Ginkgo biloba leaf-derived activated carbon	Methanol anhydrous	5	97%	93%	139
Sesame straw-derived activated carbon	0.1 M HCl	7	98%	82%	141
Waste coffee residue-derived activated carbon	Ethanol	5	69%	44%	159
Waste coffee residue-derived activated carbon	0.1 M EDTA	5	69%	15%	159
Waste coffee residue-derived activated carbon	0.1 M NaOH	5	69%	19%	159
Tamarind seed-derived activated biochar	0.4 M ethanol in water	4	89%	80%	158
Seed pods of *Erythrina speciosa*-derived activated carbon	0.5 M NaOH	7	80%	80%	152
Spent tea leaf-derived activated carbon	Ethanol	7	99%	82%	171
Terminalia catappa shell-derived activated biochar	Methanol	5	80%	60%	172
Terminalia catappa shell-derived activated biochar	Methanol	5	88%	64%	172
Tamarindus indica seed-derived activated biochar	0.6 M methanol in water	5	89%, equivalent to 23 mg g^{-1}	38%, equivalent to 16 mg g^{-1}	173
Tamarindus indica seed-derived activated biochar	0.1 M methanol in water	5	87%	57%	137

and 532.3 eV of O 1s) post-adsorption of ibuprofen. This finding presumed the presence of hydrogen bonding interaction between O of the hydroxyl groups of magnetic activated waste coffee residue biochar and H of the carboxylic groups of ibuprofen drug. Apart from XPS analysis, FTIR spectroscopic analysis was used to monitor the peak change of functional groups. For example, ibuprofen adsorption onto *Tamarindus indica* seed-derived activated biochar *via* hydrogen bonding was examined.[137] In this study, the authors observed the band shifts (*e.g.*, O–H stretch at 3446 cm^{-1}) and new peaks (*e.g.*, N–O at 1525 cm^{-1}, C–H at 1371 cm^{-1} and C–N at 1224 cm^{-1}), which confirmed hydrogen bonding with activated biochar.

To confirm the contribution of pore-filling in this mechanism, BET surface area analysis of the adsorbent before and after ibuprofen adsorption can be used. Shin *et al.* found a significant reduction in the BET surface area of magnetic activated waste coffee residue biochar from 950 $m^2\ g^{-1}$ to 142 $m^2\ g^{-1}$ and in pore volume from 0.42 $cm^3\ g^{-1}$ to 0.12 $cm^3\ g^{-1}$.[159] After adsorption, ibuprofen occupied empty micropores and mesopores of this adsorbent, causing an effect, called "pore-filling". Show *et al.* stated the decrease in pore size of *Tamarindus indica* seed-derived activated biochar from 640 nm (before adsorption) to 200 nm (after adsorption) using SEM analysis.[137] They concluded that pore-filling could be a contributor to ibuprofen adsorption.

Several studies propose multiple adsorption mechanisms for ibuprofen uptake but lack corresponding analytical evidence (Table 10). This limitation should be addressed to give the convincing assumptions of adsorption mechanism. For example, pods of *Erythrina speciosa*-derived activated carbon for ibuprofen adsorption were suggested by hydrogen bonding, π–π interactions, or π–anion interactions.[165] Nevertheless, the authors did not verify characterization data (*e.g.*, FTIR or XPS) before and after adsorption to substantiate these claims. Similarly, sunflower seed shell-derived activated carbon is reported to involve π–π interactions, hydrogen bonding, and pore-filling.[138] However, the absence of post-adsorption analysis leaves these mechanisms speculative. Other examples include *Radix Angelica Dahurica* residue-derived and sesame straw-derived activated carbons for ibuprofen adsorption.[170] Both works presumed that the presence of hydrogen bonding, electrostatic interactions, and π–π interactions between ibuprofen and activated adsorbent yet failed to present confirmatory evidence. This lack of analytical support poses significant disadvantages including undermining the scientific rigor of the findings, reducing reproducibility, and hindering a mechanistic understanding of the adsorption process. In the absence of clear evidence, *i.e.*, spectroscopic or textural alteration of the adsorbent, these studies rely heavily upon theoretical speculation based on pH relationships (*e.g.*, pK_a < pH < pH_{pzc}). This

Table 10 Mechanism of ibuprofen adsorption onto adsorbents derived from bio-wastes

Adsorbent	All adsorption mechanisms mentioned	Evidences	Ref.
Pods of the *Erythrina speciosa*-derived activated carbon	Hydrogen bond, π–π interaction, or π–anion interaction	- At optimal pH = 3: pH < pK_a, ibuprofen is neutral and electrostatic interaction did not occur - No evidence for the characterization of activated carbon before and after ibuprofen adsorption	165
Ginkgo biloba fallen leaf-derived activated carbon	Hydrogen bonding is the primary mechanism	- At optimal pH 3 < pH_{pzc} and pK_a, electrostatic interaction did not occur and hydrogen bonding could occur between adsorbent surface and ibuprofen - No evidence for the characterization of activated carbon before and after ibuprofen adsorption	139
Sunflower seed shell-derived activated carbon	π–π interaction, hydrogen bond, pore-filling	- pK_a < optimal pH < pH_{pzc}, adsorbent surface was negatively charged and ibuprofen was in an anionic form; therefore, electrostatic interaction could not occur. Thus, π–π interaction, hydrogen bond, and pore-filling could occur - No evidence for the characterization of activated carbon before and after ibuprofen adsorption	138
Radix Angelica Dahurica residue-derived activated carbon	Hydrogen bonding, electrostatic interaction, π–π interaction, and pore-filling	- At pK_a < optimal pH < pH_{pzc} < 7.2, the adsorbent surface was positively charged and ibuprofen was in an anionic form. Thus, electrostatic interaction was formed - No evidence for the characterization of activated carbon before and after ibuprofen adsorption	170
Sesame straw-derived activated carbon	Hydrogen bond, π–π interaction, electrostatic interaction	- At pK_a < optimal pH < pH_{pzc} < 7.5, the adsorbent surface was positively charged and ibuprofen anion was in an anionic form. Thus, electrostatic interaction was formed - No evidence for the characterization of activated carbon before and after ibuprofen adsorption	141
Waste coffee residue-derived activated carbon	Pore-filling, hydrogen bonding, and π–π interaction	- XPS of activated carbon after ibuprofen adsorption confirmed an increased intensity of the C=O (carbonyl) peaks at 287 eV in the C 1s spectrum and 532 eV at O 1s spectrum. This confirmed the formation of hydrogen bonding and π–π interactions - The surface area and pore volume of activated carbon were significantly decreased after the adsorption. The pore-filling effect was confirmed by the decrease in the surface area from 950 to 142 $cm^3 g^{-1}$ and the decrease in the pore volume from 0.42 to 0.12 $cm^3 g^{-1}$	159

Table 10 (*Contd.*)

Adsorbent	All adsorption mechanisms mentioned	Evidences	Ref.
Yeast milk residue-derived activated carbon	Electrostatic interactions, dipole–dipole interactions	- pK_a < the pH solution (5.3) < pH_{pzc} 7.5, the adsorbent surface was positivelt charged and ibuprofen was in an anionic form. Thus, electrostatic interaction was formed - The critical dimension of ibuprofen (0.72 nm) limited the diffusion into the narrower micropores (0.41 $cm^3\ g^{-1}$) of activated carbon	145
Spent coffee waste-derived activated carbon	Hydrophobic interaction, π–π interaction	- No evidence for the characterization of activated carbon before and after ibuprofen adsorption	161
Seed pods of the *Erythrina speciosa*-derived activated carbon	Cation–π interaction, hydrogen interaction	- pK_a and pH_{pzc} < pH solution at 3, the surface of adsorbent was positively charged. Thus, cation–π interactions occurred - No evidence for the characterization of activated carbon before and after ibuprofen adsorption	152
Tamarindus indica seed-derived activated biochar	Hydrogen bond, pore diffusion	- After adsorption, FTIR band shifts indicated ion exchange between ibuprofen and the adsorbent. The O–H stretch slightly shifted to 3446 cm^{-1}, which suggested free alcoholic groups of ibuprofen interacting with active sites of adsorbent. Several sharp peaks were present at 1525 cm^{-1} for N–O and at 1445–1224 cm^{-1} for C–H and C–N, confirming the formation of hydrogen bond with activated carbon - Pore size decreased after adsorption from 640 nm to 200 nm, which confirmed the pore diffusion effect	137

confirmation alone is insufficient to validate complex interactions.

4.7. Comparison with other adsorbents

The adsorption capacities of bio-waste-derived activated carbons from Table 6 and various other adsorbents from Table 11 for ibuprofen removal reveal distinct performance ranges influenced by different materials. Table 6 shows that activated adsorbents derived from biowaste exhibited a capacity range of 38 to 491 mg g^{-1}. Markedly, several bio-waste-derived activated carbons showed great performance for ibuprofen adsorption, such as *Phyllostachys edulis* with a Q_{max} of 491 mg g^{-1},[142] *Schizolobium parahyba* at 447 mg g^{-1},[148] and Red Mombin seeds at 339 mg g^{-1}.[133] For various adsorbents mentioned in Table 11, the maximum adsorption capacity for ibuprofen ranges from 4.4 to 512 mg g^{-1}. The highest adsorption capacities include chitosan/polyethyleneimine/$Ti_3C_2T_x$ MXene at 512 mg g^{-1},[180] and Zr-MOF-NH_2 at 371 mg g^{-1},[181] often linked to their high surface areas, such as 2150 $m^2\ g^{-1}$ for UiO-67,[182] or 730 $m^2\ g^{-1}$ for Zr-MOF-NH_2.[181] The ibuprofen adsorption capacities of graphene-based adsorbents ranged from 36 to 161 mg g^{-1}, those of polymer-based adsorbents ranged from 4.4 to 210 mg g^{-1}, those of multi-walled carbon nanotube-based adsorbents ranged from 12 to 19 mg g^{-1}, and those of clay-based adsorbents ranged from 25 to 138 mg g^{-1}. Bio-waste-derived activated carbons achieve comparable capacities, while this approach also offers sustainability benefits, *e.g.*, use of the waste raw for input and requirement of fewer chemicals for the procedures. These advantages make them viable alternatives to advanced synthetic materials.

5. Future prospects and limitations

As a remarkable prospect, the preparation of affordable and effective magnetic materials (MFe_2O_4/AC, where M = Ni, Co, Fe, and Mn, as shown in Section 3.2) from many waste resources

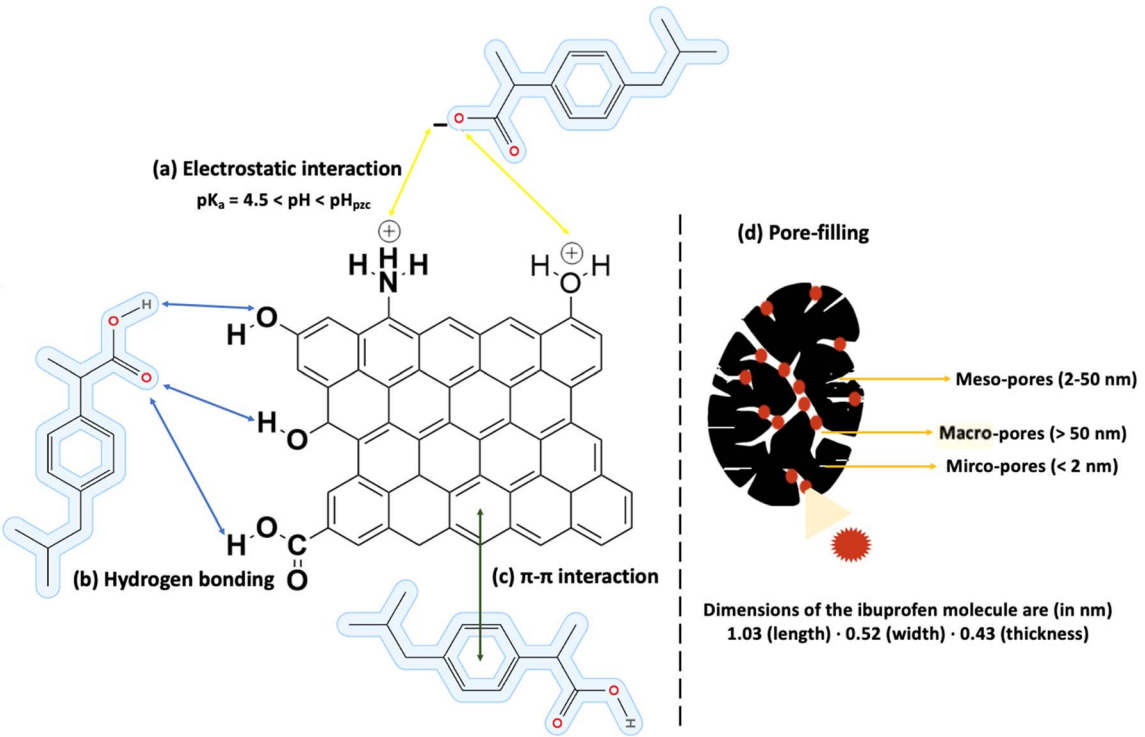

Fig. 4 Ibuprofen adsorption mechanisms of activated carbon are proposed, including (a) electrostatic interaction, (b) hydrogen bonding, (c) π–π interaction, and (d) pore-filling. The dimension of ibuprofen is reprinted with permission from ref. 179 Copyright (2007), Elsevier.

can bring a circular economy. Compared with biochars and activated carbons, the advantages of magnetic nanomaterials from waste resources are their easiness in separation, recovery, and effectiveness. This strategy can simultaneously eliminate two problems, namely, bio-waste and environmental pollution. For example, Osman *et al.* synthesized a magnetic composite from a precursor mixture of plastic waste and pomace leaf biomass for crystal violet dye treatment.[196] Through life cycle assessment, the authors revealed that the abiotic depletion of fossil fuels was 7.17 MJ and the global warming potential was 0.63 kg CO_2 equivalent for each kilogram of pomace leaves used. Thus, the production of magnetic adsorbents from combined plastic and biowastes for environmental remediation can be a future prospect for sustainable development goals (SDGs).

Table 11 Comparison of ibuprofen adsorption among various adsorbents

Type or class of adsorbents	Adsorbent	Optimal pH	S_{BET} (m^2 g^{-1})	Q_{max} (mg g^{-1})	Ref.
Multi-walled carbon nanotube-based adsorbents	Magnetic carboxylic multi-walled carbon nanotube	3.5	51	19	183
Multi-walled carbon nanotube-based adsorbents	Multi-walled carbon nanotube/hydrazine	4	187	12	184
Graphene-based adsorbents	Reduced graphene oxide-modified activated carbon	7	966	161	185
Graphene-based adsorbents	Graphene oxide-activated carbon	—	157	36	186
Polymer-based adsorbents	Chitosan/molecularly imprinted polymer/Fe	5	30	35	187
Polymer-based adsorbents	TiO_2/molecularly imprinted polymer	4	39	4.4	188
Polymer-based adsorbents	Polydopamine imprinted polymers with fluorescent carbon dots	7	184	210	189
Metal–organic frameworks	Zr-MOF-NH_2	4	730	371	181
Metal–organic frameworks	Gelatin/UiO-66/sepiolite	7	41	10	190
Metal–organic frameworks	UiO-67	6	2150	135	182
Metal oxides	ZnO nanoparticles	6	119	266	191
MXene-based adsorbents	Chitosan/polyethyleneimine/$Ti_3C_2T_x$ MXene	5	103	512	180
MXene-based adsorbents	$Ti_3C_2T_x$ MXene	7	—	214	192
Natural clay-based adsorbents	Natural clay	4	—	138	193
Clay-based adsorbents	Organobentonite	7	7	25	194
Clay-based adsorbents	C18-Mt	6.5	—	64	195

Despite some insights into ibuprofen remediation by bio-waste-derived activated adsorbents, there are some notable limitations. First, while the review considerably elaborated on adsorption kinetics, isotherms, thermodynamics, and RSM optimization, limited discussions on the practical wastewater matrices were addressed. This is due to the fact that most published works were carried out under controlled laboratory environments rather than under natural conditions. Similarly, there are very few studies reporting the simulated effluent treatment. For example, Franco *et al.* used porous carbons derived from *Erythrina speciosa* pods to remove 65.5% pharmaceuticals in a simulated effluent sample.[152] Ionic competition was a vital effect, but was rarely investigated. For example, Sohrabian *et al.* only conducted ibuprofen adsorption in the presence of 20–100 mg per L Ca^{2+} ions.[141] The effect of other common ions such as heavy metal ions (Cu^{2+}, Zn^{2+}, Fe^{2+}, *etc.*) and anionic ions (NO_3^-, NO_2^-, Cl^-, SO_4^{2-}, CO_3^{2-}, PO_4^{3-}, *etc.*) seems to be ignored. As a result, the entire interaction of the components in actual wastewater systems cannot be guaranteed under such studies. Second, the use of toxic elution agents, *e.g.*, NaOH and methanol for regeneration is harmful to the environment. Residual NaOH solutions need to be neutralized, while the recovery of methanol is more complex. Alternative solvents or solution such as H_2O and NaCl may be safer, but the desorption efficiency should be investigated. Although the thermal treatment was proposed as an alternative, the energy demand of this process as well as the deactivation of the surface-active sites on the adsorbent was not thoroughly evaluated. Third, the adsorption mechanisms evaluated in Section 4.6 often lack robust analytical support. Indeed, many studies rarely presented post-adsorption characterization data (*e.g.*, FTIR or XPS) for the validation of proposed interactions, including hydrogen bonding and π–π stacking. Such over-reliance on putative mechanisms dilutes the understanding of ibuprofen adsorption. Next, almost studies did not report how to employ salt recovery, *e.g.*, $ZnCl_2$, $FeCl_3$ and treatment of phosphorus or zinc residues after the synthesis of AC and magnetic porous carbons. These shortages should be addressed to avoid secondary pollution. Lastly, the studies rarely covered the life cycle and techno-economic assessments to indicate how the porous carbon production processes are commercially profitable or not. These assessments are also critical to expand the use of porous carbon production in industrial applications.[197]

Section 4.3 illustrates that most studies evaluating the thermodynamics of activated carbon for ibuprofen adsorption have relied on calculating the thermodynamic equilibrium constant (K_d) from eqn (4) and (5). However, the equations have been discovered to be incorrect in describing the nature of thermodynamic reactions.[198] Unfortunately, some researchers have incorrectly used these equations to calculate the thermodynamics of ibuprofen adsorption.[137,141,156–158] This drawback led to erroneous conclusions about the adsorption process. A more accurate approach for determining the standard thermodynamic equilibrium constant involves eqn (6), which was proven.[198–201] This right equation complies with the principles of physical-chemistry of equilibrium for the calculation of thermodynamic parameters of solid–liquid phase adsorption.[198] Future studies on activated carbon for ibuprofen adsorption should adopt this corrected thermodynamic equation to ensure scientific rigor. Such advances significantly increase the validity of scholarly research and enable the design of high-performance adsorbents. By the incorporation of correct analyses, activated carbon can be optimized for efficient ibuprofen removal, enabling more applications in water treatment:

$$K_d = \frac{q_e}{C_e} \times \frac{m}{V} \tag{4}$$

$$K_d = \frac{q_e}{C_e} \tag{5}$$

where q_e is the sorption capacity (mg g^{-1}) at the equilibrium, C_e is the equilibrium concentration (mg L^{-1}), m is the mass of adsorbent (g), and V is the volume of adsorbate solution (L).

$$\frac{1000 \times K_g \times \text{molecule weight of adsorbate} \times [\text{adsorbate}]^\circ}{\gamma} = \frac{K_e}{\gamma} = K_e^\circ \tag{6}$$

where γ is the activity coefficient of ibuprofen (adsorbate) (dimensionless), K_e is derived from the molar concentration of ibuprofen (dimensionless), K_g is the equilibrium constant of isotherm model (Liu, Sips, Langmuir, *etc.*) (L mg^{-1}), and [adsorbate]° is the standard concentration of the adsorbate (mol L^{-1}).

6. Conclusion

This review examined ibuprofen pollution and its effect on plants, animals and humans. Ibuprofen is found in river, wetland, surface water, ground water, and sewage water at various concentrations. H_3PO_4, $ZnCl_2$, and K_2CO_3 are the most effective activators for the fabrication of activated carbons from biowaste. The adsorption of ibuprofen on activated carbon and magnetic activated carbons produced from biowaste was mostly described by the pseudo-second-order model and the Langmuir model. The desorption of ibuprofen from bio-waste-derived adsorbents could be conducted by the use of various elution agents such as NaOH, ethanol, ethanol, and EDTA. H bonding, π–π interactions, electrostatic interactions, pore-filling, hydrophobic interactions, cation–π interactions, and dipole–dipole interactions could be the main ibuprofen adsorption mechanisms. There are some limitations related to the removal of ibuprofen in real wastewater treatment systems and the

calculation of thermodynamic parameters. Finally, this work provides insights into the synthesis and application of activated carbons and magnetic activated carbons for the removal of ibuprofen from water.

Conflicts of interest

The authors declare that there are no conflicts of interest.

Data availability

The data supporting this article have been included as part of the supplementary information (SI). Supplementary information is available. See DOI: https://doi.org/10.1039/d6na00167j.

Acknowledgements

The authors acknowledge Nguyen Tat Thanh University, Ho Chi Minh City, Vietnam, for supporting this study.

References

1 M.-W. Ha and S.-M. Paek, *Molecules*, 2021, **26**, 4792.
2 A. I. Osman, A. Ayati, M. Farghali, P. Krivoshapkin, B. Tanhaei, H. Karimi-Maleh, E. Krivoshapkina, P. Taheri, C. Tracey, A. Al-Fatesh, I. Ihara, D. W. Rooney and M. Sillanpaä, *Environ. Chem. Lett.*, 2024, **22**, 373–418.
3 S. Show, P. Chakraborty, B. Karmakar and G. Halder, *Sci. Total Environ.*, 2021, **786**, 147327.
4 S. Divya Lakshmi, B. Vijaya Geetha and V. Murali, *Toxic. Report.*, 2024, **13**, 101775.
5 G. Pooja, P. Senthil Kumar, B. Chitra and G. Rangasamy, *Int. J. Chem. Eng.*, 2024, **2024**(1), 9014776.
6 N. S. P. Batucan, L. A. Tremblay, G. L. Northcott and C. D. Matthaei, *Environ. Adv.*, 2022, **7**, 100164.
7 M. N. H. Rozaini, N.-F. Semail, Z. U. Zango, J. W. Lim, N. Yahaya, H. D. Setiabudi, W.-Y. Tong, R. Shamsuddin, Y. J. Chan, K. S. Khoo, M. Suliman and W. Kiatkittipong, *J. Taiwan Inst. Chem. Eng.*, 2025, **166**, 105020.
8 P. Mikula, A. Hollerova, N. Hodkovicova, V. Doubkova, P. Marsalek, A. Franc, L. Sedlackova, R. Hesova, H. Modra, Z. Svobodova and J. Blahova, *Sci. Total Environ.*, 2024, **917**, 170296.
9 I. Nassri, S. khattabi rifi, F. Sayerh and S. Souabi, *Environ. Nanotechnol. Monit. Manage.*, 2023, **20**, 100878.
10 D. Chen, M. Li, Y. Li, S. Long, X. Sun, H. Geng, M. Yin, Y. Yang and L. Zhao, *J. Water Process Eng.*, 2024, **57**, 104599.
11 I. Ambriz-Mexicano, S. González-Juárez, N. Ruiz-Ordaz, J. Galíndez-Mayer, F. Santoyo-Tepole, C. Juárez-Ramírez and M. Galar-Martínez, *Bioprocess Biosyst. Eng.*, 2022, **45**, 1547–1557.
12 S. H. Lee, S. Annamalai and W. S. Shin, *Environ. Pollut.*, 2023, **322**, 121023.
13 G. Kooijman, M. K. de Kreuk, C. Houtman and J. B. van Lier, *J. Water Process Eng.*, 2020, **34**, 101161.
14 M. Zhu, M. Zhang, Y. Yuan, P. Zhang, S. Du, T. Ya, D. Chen, X. Wang and T. Zhang, *J. Environ. Manage.*, 2021, **289**, 112473.
15 M. Negarestani, S. Reisi, M. Sohrabi, H. Shayesteh, H. Farimaniraad, A. Mollahosseini, M. Hosseinzadeh and S. Tavassoli, *J. Water Process Eng.*, 2024, **57**, 104657.
16 P. Alfonso-Muniozguren, E. A. Serna-Galvis, M. Bussemaker, R. A. Torres-Palma and J. Lee, *Ultrason. Sonochem.*, 2021, **76**, 105656.
17 D. Pereira, M. V. Gil, V. I. Esteves, N. J. O. Silva, M. Otero and V. Calisto, *J. Hazard. Mater.*, 2023, **443**, 130258.
18 B. Wang, J. Lan, C. Bo, B. Gong and J. Ou, *RSC Adv.*, 2023, **13**, 4275–4302.
19 A. Arul, S. Kavitha, A. Anand Babu Christus, V. J. Surya, A. Ravikumar and Y. Sivalingam, *Surf. Interfaces*, 2023, **40**, 103095.
20 G. Weldesemayat Sileshi, E. Barrios, J. Lehmann and F. N. Tubiello, *Earth Syst. Sci. Data*, 2025, **17**, 369–391.
21 G. D. Gebre, S. N. Gebremariam, Y. G. Keneni and J. M. Marchetti, *Biofuel Bioprod. Biorefining*, 2023, **17**, 1807–1842.
22 S. Mor and K. Ravindra, *Process Saf. Environ. Prot.*, 2023, **174**, 510–530.
23 H. Adamu, U. Bello, A. U. Yuguda, U. I. Tafida, A. M. Jalam, A. Sabo and M. Qamar, *Renew. Sustain. Energy Rev.*, 2023, **186**, 113686.
24 A. Ayati, B. Tanhaei, H. Beiki, P. Krivoshapkin, E. Krivoshapkina and C. Tracey, *Chemosphere*, 2023, **323**, 138241.
25 H. Rashid Ahmed, K. F. Kayani, A. Mary Ealias and G. George, *Inorg. Chem. Commun.*, 2024, **170**, 113397.
26 A. Esmaeili Nasrabadi, B. Ramavandi and Z. Bonyadi, *Environ. Sci. Pollut. Res.*, 2025, **33**(13), 5795–5817.
27 F. A. Ahmad, *Heliyon*, 2023, **9**, e16449.
28 J. M. Castaño-Ortiz, R. Gil-Solsona, N. Ospina-Álvarez, J. D. Alcaraz-Hernández, M. Farré, V. M. León, D. Barceló, L. H. M. L. M. Santos and S. Rodríguez-Mozaz, *Sci. Total Environ.*, 2024, **906**, 167467.
29 A. Cerón-Vivas and G. A. Peñuela Mesa, *Environ. Res.*, 2024, **252**, 118951.
30 R. F. do Nascimento, J. A. A. de Carvalho Filho, D. C. Napoleão, B. G. Ribeiro, J. J. da Silva Pereira Cabral and A. L. R. de Paiva, *Water, Air, Soil Pollut.*, 2023, **234**, 225.
31 J. Antos, J. Zembrzuska, J. Jeż-Walkowiak, A. Makała, D. Ginter-Kramarczyk, I. Kruszelnicka and F. Uwimpaye, *Water*, 2023, **15**, 2716.
32 D. T. Adedipe, C. Chen, R. W. S. Lai, S. Xu, Q. Luo, G.-J. Zhou, A. Boxall, B. W. Brooks, M. A. Doblin, X. Wang, J. Wang and K. M. Y. Leung, *Environ. Int.*, 2024, **192**, 109031.
33 M. U. Rehman, B. Nisar, A. Mohd Yatoo, N. Sehar, R. Tomar, L. Tariq, S. Ali, A. Ali, S. Mudasir Rashid, S. Bilal Ahmad and R. M. Aldossari, *Sep. Purif. Technol.*, 2024, **342**, 126921.
34 G. Deryal, N. E. Korkmaz, A. Aksu, E. Başar, N. Çağlar Balkıs, C. Gazioğlu and B. Özsoy, *Turk. J. Fish. Aquat. Sci.*, 2024, **24**, 1–8.

35 N. Grujić-Letić, E. Gligorić, B. Teofilović, M. Vraneš and S. Gadžurić, *Acta Chim. Slov.*, 2023, **70**, 59–64.
36 C. Elles-Pérez, M. Guzman-Tordecilla, Y. Ramos, M. Castillo-Ramírez, A. Moreno-Ríos, C. Garzón-Rodríguez and J. Rojas-Solano, *Heliyon*, 2024, **10**, e39005.
37 C. Martínez-Megías, A. Arenas-Sánchez, D. Manjarrés-López, S. Pérez, Y. Soriano, Y. Picó and A. Rico, *Environ. Sci. Pollut. Res.*, 2024, **31**, 14593–14609.
38 A. T. de Rezende and A. H. Mounteer, *Environ. Pollut.*, 2023, **338**, 122628.
39 F. Khezami, O. Gómez-Navarro, M. V. Barbieri, N. Khiari, A. Chkirbene, S. Chiron, S. Khadhar and S. Pérez, *Sci. Total Environ.*, 2024, **906**, 167319.
40 S. Royano, A. de la Torre, I. Navarro and M. Á. Martínez, *Sci. Total Environ.*, 2023, **905**, 167422.
41 M. Digaletos, C. J. Ptacek, J. Thomas and Y. Liu, *Sci. Total Environ.*, 2023, **870**, 161866.
42 C. H. Besley, G. E. Batley and M. Cassidy, *Environ. Sci. Pollut. Res.*, 2023, **30**, 96763–96781.
43 A. Dawood, D. S. Drage, S. Harrad and M. A.-E. Abdallah, *Environ. Pollut Manag.*, 2024, **1**, 87–98.
44 E. P. Munzhelele, W. B. Ayinde, W. M. Gitari, G. K. Pindihama and R. Mudzielwana, *Heliyon*, 2025, **11**, e41524.
45 B. E. Dankwa, B. A. Nyaaba, G. Amenuvor, S. Obiri-Yeboah, G. Darko, M. K. Laryea and L. S. Borquaye, *Essent. Chem*, 2024, **1**, 1–12.
46 K. Placová, S. Heviánková, J. Halfar, K. Brožová, O. Motyka, K. Čabanová, S. Drabinová and J. Chromíková, *J. Hazard. Mater. Adv.*, 2024, **16**, 100477.
47 S. Fekadu, E. Alemayehu, R. Dewil and B. Van der Bruggen, *Sci. Total Environ.*, 2019, **654**, 324–337.
48 J. L. Wilkinson, A. B. A. Boxall, D. W. Kolpin, K. M. Y. Leung, R. W. S. Lai, C. Galbán-Malagón, A. D. Adell, J. Mondon, M. Metian, R. A. Marchant, A. Bouzas-Monroy, A. Cuni-Sanchez, A. Coors, P. Carriquiriborde, M. Rojo, C. Gordon, M. Cara, M. Moermond, T. Luarte, V. Petrosyan, Y. Perikhanyan, C. S. Mahon, C. J. McGurk, T. Hofmann, T. Kormoker, V. Iniguez, J. Guzman-Otazo, J. L. Tavares, F. Gildasio De Figueiredo, M. T. P. Razzolini, V. Dougnon, G. Gbaguidi, O. Traoré, J. M. Blais, L. E. Kimpe, M. Wong, D. Wong, R. Ntchantcho, J. Pizarro, G.-G. Ying, C.-E. Chen, M. Páez, J. Martínez-Lara, J.-P. Otamonga, J. Poté, S. A. Ifo, P. Wilson, S. Echeverría-Sáenz, N. Udikovic-Kolic, M. Milakovic, D. Fatta-Kassinos, L. Ioannou-Ttofa, V. Belušová, J. Vymazal, M. Cárdenas-Bustamante, B. A. Kassa, J. Garric, A. Chaumot, P. Gibba, I. Kunchulia, S. Seidensticker, G. Lyberatos, H. P. Halldórsson, M. Melling, T. Shashidhar, M. Lamba, A. Nastiti, A. Supriatin, N. Pourang, A. Abedini, O. Abdullah, S. S. Gharbia, F. Pilla, B. Chefetz, T. Topaz, K. M. Yao, B. Aubakirova, R. Beisenova, L. Olaka, J. K. Mulu, P. Chatanga, V. Ntuli, N. T. Blama, S. Sherif, A. Z. Aris, L. J. Looi, M. Niang, S. T. Traore, R. Oldenkamp, O. Ogunbanwo, M. Ashfaq, M. Iqbal, Z. Abdeen, A. O'Dea, J. M. Morales-Saldaña, M. Custodio, H. de la Cruz, I. Navarrete, F. Carvalho, A. B. Gogra, B. M. Koroma, V. Cerkvenik-Flajs, M. Gombač, M. Thwala, K. Choi, H. Kang, J. L. C. Ladu, A. Rico, P. Amerasinghe, A. Sobek, G. Horlitz, A. K. Zenker, A. C. King, J.-J. Jiang, R. Kariuki, M. Tumbo, U. Tezel, T. T. Onay, J. B. Lejju, Y. Vystavna, Y. Vergeles, H. Heinzen, A. Pérez-Parada, D. B. Sims, M. Figy, D. Good and C. Teta, *Proc. Natl. Acad. Sci. U. S. A.*, 2022, **119**(8), e2113947119.
49 V. Menicagli, M. Ruffini Castiglione, E. Cioni, C. Spanò, E. Balestri, M. De Leo, S. Bottega, C. Sorce and C. Lardicci, *J. Hazard. Mater.*, 2024, **476**, 135188.
50 L. Wijaya, M. Alyemeni, P. Ahmad, A. Alfarhan, D. Barcelo, M. A. El-Sheikh and Y. Pico, *Plants*, 2020, **9**, 1–14.
51 A. C. Barbera, G. Leonardi, M. Ferrante, P. Zuccarello and C. Maucieri, *Agric. Water Manag.*, 2020, **232**, 106005.
52 F. Pietrini, D. Di Baccio, J. Aceña, S. Pérez, D. Barceló and M. Zacchini, *J. Hazard. Mater.*, 2015, **300**, 189–193.
53 D. Rede, L. H. M. L. M. Santos, S. Ramos, F. Oliva-Teles, C. Antão, S. R. Sousa and C. Delerue-Matos, *Chemosphere*, 2016, **159**, 193–198.
54 Y. Picó, R. Alvarez-Ruiz, L. Wijaya, A. Alfarhan, M. Alyemeni and D. Barceló, *Anal. Bioanal. Chem.*, 2018, **410**, 1163–1176.
55 R. I. Sha'aba, M. A. Chia, Y. A. Gana, A. B. Alhassan and I. M. K. Gadzama, *Environ. Sci. Pollut. Res.*, 2022, **30**, 13118–13131.
56 V. Martyniuk, V. Khoma, T. Matskiv, V. Baranovsky, K. Orlova-Hudim, B. Gylytė, R. Symchak, O. Matciuk, L. Gnatyshyna, L. Manusadžianas and O. Stoliar, *Comp. Biochem. Physiol., Part C: Toxicol. Pharmacol.*, 2022, **261**, 109425.
57 A.-B. Muñiz-González, *Environ. Toxicol. Pharmacol.*, 2021, **81**, 103537.
58 W. Jiang, Z. Zhao, Q. Zhao, X. He, H. Chen, G. Wu and X.-X. Zhang, *Environ. Sci. Technol.*, 2025, **59**, 756–766.
59 Z. Beitgader, N. Salamat, M. A. Salarialiabadi, H. Mojiri-Forushani and A. Mohammadi, *Toxicol. Vitro*, 2025, **104**, 106008.
60 F. T. Mathias, D. H. Fockink, G. R. Disner, V. Prodocimo, J. L. C. Ribas, L. P. Ramos, M. M. Cestari and H. C. Silva de Assis, *Environ. Toxicol. Pharmacol.*, 2018, **59**, 105–113.
61 N. Veldhoen, R. C. Skirrow, L. L. Y. Brown, G. van Aggelen and C. C. Helbing, *Environ. Sci. Technol.*, 2014, **48**, 10439–10447.
62 K. T. Cosgrove, R. Kuplicki, J. Savitz, K. Burrows, W. K. Simmons, S. S. Khalsa, T. K. Teague, R. L. Aupperle and M. P. Paulus, *Brain Behav. Immun.*, 2021, **96**, 135–142.
63 A. Kulesza, K. Zielniok, J. Hawryluk, L. Paczek and A. Burdzinska, *Biomolecules*, 2022, **12**, 287.
64 X. Chen, D. Han, X. Wang, X. Huang, Z. Huang, Y. Liu, J. Zhong, F. J. Walther, C. Yang and G. T. M. Wagenaar, *Respir. Res.*, 2023, **24**, 39.
65 P. Hurtado-Gonzalez, R. A. Anderson, J. Macdonald, S. van den Driesche, K. Kilcoyne, A. Jørgensen, C. McKinnell, S. Macpherson, R. M. Sharpe and R. T. Mitchell, *Environ. Health Perspect.*, 2018, **126**, 047006.
66 D. M. Kristensen, C. Desdoits-Lethimonier, A. L. Mackey, M. D. Dalgaard, F. De Masi, C. H. Munkbøl, B. Styrishave,

J.-P. Antignac, B. Le Bizec, C. Platel, A. Hay-Schmidt, T. K. Jensen, L. Lesné, S. Mazaud-Guittot, K. Kristiansen, S. Brunak, M. Kjaer, A. Juul and B. Jégou, *Proc. Natl. Acad. Sci. U. S. A.*, 2018, **115**, E715–E724.
67 I. Neme, G. Gonfa and C. Masi, *Heliyon*, 2022, **8**, e11940.
68 J. Missau, D. A. Bertuol and E. H. Tanabe, *Appl. Clay Sci.*, 2021, **214**, 106297.
69 O. Oginni, K. Singh, G. Oporto, B. Dawson-Andoh, L. McDonald and E. Sabolsky, *Bioresour. Technol. Rep.*, 2019, **8**, 100307.
70 J. Liang, C. Li, S. Zhang, B. A. Mohamed, L. Wang, J. Xiang, S. Hu, Y. Wang and X. Hu, *Fuel Process. Technol.*, 2023, **252**, 107986.
71 J. Liang, C. Li, S. Zhang, S. Wang and X. Hu, *Ind. Crops Prod.*, 2024, **221**, 119387.
72 I. Neme, G. Gonfa and C. Masi, *Results Mater.*, 2022, **15**, 100304.
73 I. S. Ismail, N. A. Rashidi and S. Yusup, *Environ. Sci. Pollut. Res.*, 2022, **29**, 12434–12440.
74 A. H. Jawad, N. N. Mohd Firdaus Hum, A. S. Abdulhameed and M. A. Mohd Ishak, *Int. J. Environ. Anal. Chem.*, 2022, **102**, 6061–6077.
75 M. Danish, Z. Pin, L. Ziyang, T. Ahmad, S. Majeed, A. N. Ahmad Yahya, W. A. Khanday and H. P. S. Abdul Khalil, *Mater. Chem. Phys.*, 2022, **282**, 125989.
76 W. Zhao, L. Chen and Y. Jiao, *Water Sci. Eng.*, 2023, **16**, 192–202.
77 F. Mbarki, T. Selmi, A. Kesraoui and M. Seffen, *Ind. Crops Prod.*, 2022, **178**, 114546.
78 M. G. Alam, M. Danish, A. M. Alanazi, T. Ahmad and H. P. S. A. Khalil, *Diam. Relat. Mater.*, 2023, **132**, 109632.
79 M. Fan, Y. Shao, Y. Wang, J. Sun, H. He, Y. Guo, S. Zhang, S. Wang, B. Li and X. Hu, *Renewable Energy*, 2025, **240**, 122151.
80 S. Wei, Q. Qin and Z. Liu, *J. Anal. Appl. Pyrolysis*, 2024, **179**, 106500.
81 G. Zhang, H. Yang, M. Jiang and Q. Zhang, *Colloids Surf., A*, 2022, **641**, 128124.
82 M. Fan, Y. Shao, Y. Wang, J. Sun, H. He, Y. Jiang, S. Zhang, Y. Wang and X. Hu, *Chem. Eng. J.*, 2024, **500**, 157278.
83 E. R. Raut, M. A. Bedmohata and A. R. Chaudhari, *Mater. Today Proc.*, 2022, **66**, 1875–1884.
84 D. Bosch, J. O. Back, D. Gurtner, S. Giberti, A. Hofmann and A. Bockreis, *Carbon Resour. Convers.*, 2022, **5**, 299–309.
85 L. Kong, C. Li, R. Sun, S. Zhang, Y. Wang, J. Xiang, S. Hu, D. Wang, C. Leng and X. Hu, *Chin. J. Chem. Eng.*, 2024, **69**, 227–237.
86 D. A. Khuong, K. T. Trinh, Y. Nakaoka, T. Tsubota, D. Tashima, H. N. Nguyen and D. Tanaka, *Chemosphere*, 2022, **299**, 134365.
87 Y. Xu, Y. Liu, W. Zhan, D. Zhang, Y. Liu, Y. Xu and Z. Wu, *Biomass Bioenergy*, 2024, **183**, 107148.
88 W. Wu, C. Wu, G. Zhang, J. Liu, Y. Li and G. Li, *Fuel*, 2023, **332**, 126107.
89 J. Gong, R. Liu, Y. Sun, J. Xu, M. Liang, Y. Sun and L. Long, *Ind. Crops Prod.*, 2024, **208**, 117846.
90 W. Wu, C. Wu, J. Liu, H. Yan, G. Zhang, G. Li, Y. Zhao and Y. Wang, *Fuel*, 2024, **363**, 130937.
91 P. Zhang, Y. Chen, X. Song, H. Zhang, J. Cui and B. Wang, *Chem. Eng. J.*, 2025, **503**, 157703.
92 Y. A. Teymur, F. Güzel and İ. I. G. İnal, *Diam. Relat. Mater.*, 2023, **135**, 109815.
93 Y. Zhang, X. Xu, Q. Geng, Q. Li, X. Li, Y. Wang, Z. Tang, B. Gao, X. Zhang, P. K. Chu and K. Huo, *Chem. Sci.*, 2025, **16**, 2034–2043.
94 F. Yang, L. Xing, X. Zhong, Y. Liu, Z. Guo, J. Yang, A. Yuan and J. Pan, *Sep. Purif. Technol.*, 2024, **341**, 126891.
95 H. Qian, D. Yin, B. Qin, L. Li, J. Zhu, L. Mu, C. Li, B. Dong, D. Huang and X. Lu, *Fuel*, 2022, **311**, 122516.
96 S. Zhou, A. Hu, J. Jiang, J. Tang, G. Zhou, L. Zhu and S. Wang, *Biomass Bioenergy*, 2023, **177**, 106938.
97 S. Liu, R. Ma, X. Hu, L. Wang, X. Wang, M. Radosz and M. Fan, *Ind. Eng. Chem. Res.*, 2020, **59**, 7046–7053.
98 P. Feng, J. Li, H. Wang and Z. Xu, *ACS Omega*, 2020, **5**, 24064–24072.
99 A. E. Ogungbenro, D. V. Quang, K. A. Al-Ali, L. F. Vega and M. R. M. Abu-Zahra, *J. Environ. Chem. Eng.*, 2020, **8**, 104257.
100 J. Qu, Y. Liu, L. Cheng, Z. Jiang, G. Zhang, F. Deng, L. Wang, W. Han and Y. Zhang, *J. Hazard. Mater.*, 2021, **403**, 123607.
101 O. C. Altinci and M. Demir, *Energy Fuels*, 2020, **34**, 7658–7665.
102 A. I. Osman, E. O'Connor, G. McSpadden, J. K. Abu-Dahrieh, C. Farrell, A. H. Al-Muhtaseb, J. Harrison and D. W. Rooney, *J. Chem. Technol. Biotechnol.*, 2020, **95**, 183–195.
103 Y. W. Chen and H. V. Lee, *Rev. Chem. Eng.*, 2020, **36**, 215–235.
104 Q. Zhang, E. Zhu, T. Li, L. Zhang and Z. Wang, *Biomacromolecules*, 2024, **25**, 6296–6318.
105 Q.-F. Wu and F.-S. Zhang, *Fuel*, 2012, **94**, 426–432.
106 B. Li, C. Li, D. Li, L. Zhang, S. Zhang, Z. Cui, D. Wang, Y. Tang and X. Hu, *Fuel Process. Technol.*, 2023, **252**, 107987.
107 Y. Zou, C. Liu, L. Xu, Y. Li, M. Dong, W. Kong, B. Shen, Z. Wang, X. Wang and J. Yang, *J. Power Sources*, 2024, **602**, 234333.
108 L. Wang, F. Sun, F. Hao, Z. Qu, J. Gao, M. Liu, K. Wang, G. Zhao and Y. Qin, *Chem. Eng. J.*, 2020, **383**, 123205.
109 S. I. Moussa, M. M. S. Ali and R. R. Sheha, *Chin. J. Chem. Eng.*, 2021, **29**, 135–145.
110 J. Hemalatha, M. Senthil, D. Madhan, A. M. Al-Mohaimeed and W. A. Al-onazi, *Diam. Relat. Mater.*, 2024, **144**, 110995.
111 D. T. C. Nguyen, A. A. Jalil, N. S. Hassan and M. B. Bahari, *Mater. Chem. Phys.*, 2025, **334**, 130460.
112 M. J. Livani, M. Ghorbani and H. Mehdipour, *Xinxing Tan Cailiao*, 2018, **33**, 578–586.
113 Q. Chen, J. Zheng, Q. Yang, Z. Dang and L. Zhang, *ACS Appl. Mater. Interfaces*, 2019, **11**, 15478–15488.
114 N. T. H. Nguyen, G. T. Tran, T. T. T. Nguyen, D. T. C. Nguyen and T. Van Tran, *Environ. Res.*, 2024, **254**, 118883.
115 Y. A. Teymur and F. Güzel, *J. Environ. Chem. Eng.*, 2024, **12**, 112641.
116 B. Barzegar, S. J. Peighambardoust, H. Aghdasinia and R. Foroutan, *J. Water Process Eng.*, 2023, **53**, 103803.

117 R. Askari, S. Afshin, Y. Rashtbari, A. Moharrami, F. Mohammadi, M. Vosuoghi and A. Dargahi, *J. Dispers. Sci. Technol.*, 2023, **44**, 1183–1194.
118 Z. Liao, H.-Y. Su, J. Cheng, G.-T. Sun, L. Zhu and M.-Q. Zhu, *Ind. Crops Prod.*, 2021, **171**, 113861.
119 L. P. Hoang, H. T. Van, T. T. Hang Nguyen, V. Q. Nguyen and P. Q. Thang, *J. Chem.*, 2020, **2020**, 1–12.
120 P. Wang, Y. Zhang, J. Zhu, J. Wei, J. Qi, T. Cao and M. Yang, *Chem. Eng. J.*, 2024, **492**, 151886.
121 V. Priyan V, N. Kumar and S. Narayanasamy, *Chemosphere*, 2022, **294**, 133758.
122 M. Bagherzadeh, B. Aslibeiki and N. Arsalani, *Sci. Rep.*, 2023, **13**, 3960.
123 A. Mohammadifard, D. Allouss, M. Vosoughi, A. Dargahi and A. Moharrami, *Appl. Water Sci.*, 2022, **12**, 88.
124 R. Kaveh and M. Bagherzadeh, *Diam. Relat. Mater.*, 2022, **124**, 108923.
125 J. Zuo, B. Wang, J. Kang, P. Yan, J. Shen, S. Wang, D. Fu, X. Zhu, T. She, S. Zhao and Z. Chen, *Sep. Purif. Technol.*, 2022, **297**, 121459.
126 N. A. Bakar, N. Othman, Z. M. Yunus, W. A. H. Altowayti, A. Al-Gheethi, S. M. Asharuddin, M. Tahir, N. Fitriani and S. N. A. Mohd-Salleh, *Biomass Convers. Biorefinery*, 2023, **13**, 11085–11098.
127 A. Tripathy, S. Mohanty, S. K. Nayak and A. Ramadoss, *J. Environ. Chem. Eng.*, 2021, **9**, 106398.
128 T. N. Nguyen, P. A. Le and V. B. T. Phung, *Biomass Convers. Biorefinery*, 2022, **12**, 2407–2416.
129 L. Gao, Z. Liu, Z. Yang, L. Cao, C. Feng, M. Chu and J. Tang, *Appl. Surf. Sci.*, 2020, **508**, 145292.
130 Y. Li, Y.-F. Guo, Z.-X. Li, P.-F. Wang, Y. Xie and T.-F. Yi, *Energy Storage Mater.*, 2024, **67**, 103300.
131 H. Nourmoradi, K. F. Moghadam, A. Jafari and B. Kamarehie, *J. Environ. Chem. Eng.*, 2018, **6**, 6807–6815.
132 S. S. Mayakaduwa, P. Kumarathilaka, I. Herath, M. Ahmad, M. Al-Wabel, Y. S. Ok, A. Usman, A. Abduljabbar and M. Vithanage, *Chemosphere*, 2016, **144**, 2516–2521.
133 L. Matějová, J. Bednárek, J. Tokarský, I. Koutník, B. Sokolová and G. J. F. Cruz, *Appl. Surf. Sci.*, 2022, **605**, 154607.
134 F. Mansour, M. Al-Hindi, R. Yahfoufi, G. M. Ayoub and M. N. Ahmad, *Rev. Environ. Sci. Bio/Technol.*, 2018, **17**, 109–145.
135 L. S. Rocha, D. Pereira, É. Sousa, M. Otero, V. I. Esteves and V. Calisto, *Sci. Total Environ.*, 2020, **718**, 137272.
136 A. J. R. Capistrano, R. J. D. Labadan, J. E. B. Viernes, E. M. Aragua, R. N. Palac and R. O. Arazo, *Energy Ecol. Environ.*, 2023, **8**, 101–112.
137 S. Show, S. Chowdhury, M. Maji, P. Sarkar, M. Ghosh, M. Sillanpää and G. Halder, *Biomass Convers. Biorefinery*, 2024, **14**, 11579–11600.
138 J. J. Alvear-Daza, A. Cánneva, J. A. Donadelli, M. Manrique-Holguín, J. A. Rengifo-Herrera and L. R. Pizzio, *Biomass Convers. Biorefinery*, 2023, **13**, 13197–13219.
139 Q. Su, F. Ren, Y. Zhang, Y. Wang, S. Cao, Z. Li, Y. Shen, H. Li, Y. Su, Y. Wang and J. Liang, *Ind. Crops Prod.*, 2025, **226**, 120739.
140 K. Mabalane, P. Thabede and N. Shooto, *Green Anal. Chem.*, 2024, **10**, 100135.
141 B. Sohrabian, S. Sobhanardakani, B. Lorestani, M. Cheraghi and H. Nourmoradi, *Environ. Sci. Pollut. Res.*, 2023, **30**, 104563–104576.
142 Q. Gao, L. Ni, S. Rong, S. Liu, Y. Zhong and Z. Liu, *Bioresour. Technol.*, 2024, **413**, 131546.
143 A. Riah, S. Bousba, D. Ben Salem, H. Allal, S. B. Benamira, M. D. Allam, S. Bougherara and A. Zaiter, *Surf. Interfaces*, 2025, **62**, 106134.
144 Y. Guo, D. Lu, Z. Wang and Q. Wang, *Environ. Technol. Innov.*, 2025, **37**, 104025.
145 G. Labuto, A. P. Carvalho, A. S. Mestre, M. S. dos Santos, H. R. Modesto, T. D. Martins, S. G. Lemos, H. D. T. da Silva, E. N. V. M. Carrilho and W. A. Carvalho, *Sustain. Chem. Pharm.*, 2022, **28**, 100703.
146 N. Malesic-Eleftheriadou, E. V. Liakos, E. Evgenidou, G. Z. Kyzas, D. N. Bikiaris and D. A. Lambropoulou, *J. Mol. Liq.*, 2022, **368**, 120795.
147 M. Sajid, S. Bari, M. Saif Ur Rehman, M. Ashfaq, Y. Guoliang and G. Mustafa, *Alexandria Eng. J.*, 2022, **61**, 7203–7212.
148 Y. L. D. O. Salomón, J. Georgin, D. S. P. Franco, M. S. Netto, D. G. A. Piccilli, E. L. Foletto, C. Manera, M. Godinho, D. Perondi and G. L. Dotto, *Environ. Sci. Pollut. Res.*, 2022, **29**, 21860–21875.
149 C. Vogt and B. M. Weckhuysen, *Nat. Rev. Chem.*, 2022, **6**, 89–111.
150 Z. U. Zango, A. Garba, A. Haruna, S. S. Imam, A. U. Katsina, A. F. Ali, A. Z. Abidin, M. U. Zango, Z. N. Garba, A. Hosseini-Bandegharaei, A. U. Yuguda and H. Adamu, *J. Water Process Eng.*, 2024, **67**, 106186.
151 V. Vinayagam, S. Murugan, R. Kumaresan, M. Narayanan, M. Sillanpää, D. Viet N Vo, O. S. Kushwaha, P. Jenis, P. Potdar and S. Gadiya, *Chemosphere*, 2022, **300**, 134597.
152 D. S. P. Franco, D. Pinto, J. Georgin, M. S. Netto, E. L. Foletto, C. Manera, M. Godinho, L. F. O. Silva and G. L. Dotto, *J. Environ. Chem. Eng.*, 2022, **10**, 108070.
153 M. O. Omorogie, J. O. Babalola, M. O. Ismaeel, J. D. McGettrick, T. M. Watson, D. M. Dawson, M. Carta and M. F. Kuehnel, *Adv. Powder Technol.*, 2021, **32**, 866–874.
154 N. Sivarajasekar, N. Mohanraj, S. Sivamani, J. Prakash Maran, I. Ganesh Moorthy and K. Balasubramani, *Mater. Today Proc.*, 2018, **5**, 7264–7274.
155 J. J. Alvear-Daza, J. A. Rengifo-Herrera and L. R. Pizzio, *Adsorption*, 2024, **30**, 783–800.
156 T. Xing, Y. Wu, Q. Wang, A. Sadrnia, A. Behmaneshfar and E. N. Dragoi, *Environ. Res.*, 2023, **231**, 116223.
157 I. A. Olowonyo, K. K. Salam, M. O. Aremu and A. Lateef, *Waste Manag. Bull.*, 2024, **1**, 217–233.
158 S. Show, B. Karmakar and G. Halder, *Biomass Convers. Biorefinery*, 2022, **12**, 3955–3973.
159 J. Shin, J. Kwak, S. Kim, C. Son, Y.-G. Lee, S. Baek, Y. Park, K.-J. Chae, E. Yang and K. Chon, *J. Environ. Chem. Eng.*, 2022, **10**, 107914.

160 R. L. T. Costa, R. A. do Nascimento, R. C. S. de Araújo, M. G. A. Vieira, M. G. C. da Silva, S. M. L. de Carvalho and L. J. G. de Faria, *J. Mol. Liq.*, 2021, **343**, 116980.
161 J. Shin, J. Kwak, Y. G. Lee, S. Kim, M. Choi, S. Bae, S. H. Lee, Y. Park and K. Chon, *Environ. Pollut.*, 2021, **270**, 116244.
162 E. Amirmotalebi, N. Samadi and S. Ershad, *Anal. Bioanal. Chem. Res.*, 2024, **11**, 123–137.
163 S. Mondal, K. Aikat and G. Halder, *Ecol. Eng.*, 2016, **92**, 158–172.
164 S. Oh, W. S. Shin and H. T. Kim, *Environ. Sci. Pollut. Res.*, 2016, **23**, 22882–22889.
165 M. Bouzidi, L. Sellaoui, M. Mohamed, D. S. P. Franco, A. Erto and M. Badawi, *J. Mol. Liq.*, 2023, **376**, 121457.
166 S. Mondal, K. Bobde, K. Aikat and G. Halder, *J. Environ. Manage.*, 2016, **182**, 581–594.
167 M. Zhang, Y. Huang, D. Hao, Y. Ji and D. Ouyang, *Fluid Phase Equilib.*, 2020, **510**, 112454.
168 O. A. Oyetade, B. S. Martincigh and A. A. Skelton, *J. Phys. Chem. C*, 2018, **122**, 22556–22568.
169 H. O. Orugba, C. Osagie, D. Ukpenusiowho, C. A. Igwegbe and G. O. Odigie, *Desalin. Water Treat.*, 2024, **319**, 100534.
170 J. Zhang, X. Zhang, X. Li, W. Li, S. Mao, S. He, X. Wu, C. Tang, J. Yu, L. Pan and X. Zhou, *Environ. Prog. Sustain. Energy*, 2024, **43**, e14318.
171 S. L. Wong, M. H. Mohamed Noor, N. Ngadi, I. Mohammed Inuwa, R. Mat and N. A. Saidina Amin, *Int. J. Environ. Res.*, 2021, **15**, 413–426.
172 S. Show, S. Mukherjee, M. S. Devi, B. Karmakar and G. Halder, *Process Saf. Environ. Prot.*, 2021, **147**, 942–964.
173 S. Show, R. Sarkhel and G. Halder, *Sustain. Chem. Pharm.*, 2022, **27**, 100698.
174 Z. Ma, D. Yao, J. Zhao, H. Li, Z. Chen, P. Cui, Z. Zhu, L. Wang, Y. Wang, Y. Ma and J. Gao, *Process Saf. Environ. Prot.*, 2021, **148**, 462–472.
175 V. Hessel, N. N. Tran, M. R. Asrami, Q. D. Tran, N. Van Duc Long, M. Escribà-Gelonch, J. O. Tejada, S. Linke and K. Sundmacher, *Green Chem.*, 2022, **24**, 410–437.
176 M. R. Sovizi, *J. Therm. Anal. Calorim.*, 2010, **102**, 285–289.
177 R. S. Medeiros, A. P. G. Ferreira and E. T. G. Cavalheiro, *J. Therm. Anal. Calorim.*, 2020, **142**, 849–859.
178 G. Caviglioli, P. Valeria, P. Brunella, C. Sergio, A. Attilia and B. Gaetano, *J. Pharm. Biomed. Anal.*, 2002, **30**, 499–509.
179 A. S. Mestre, J. Pires, J. M. F. Nogueira and A. P. Carvalho, *Carbon*, 2007, **45**, 1979–1988.
180 Y. Li, H. Zhang, G. Qu, L. Xie, S. Tang, H. Lei, Y. Zhong and Y.-F. Zhang, *Colloids Surf., A*, 2024, **702**, 135111.
181 N. D. Alkhathami, N. A. Alamrani, A. Hameed, S. D. Al-Qahtani, R. Shah and N. M. El-Metwaly, *Polyhedron*, 2023, **235**, 116349.
182 M. M. H. Mondol, D. K. Yoo and S. H. Jhung, *J. Environ. Chem. Eng.*, 2022, **10**, 108560.
183 X. Zhang, C. Gao, R. Wang and R. Han, *J. Environ. Chem. Eng.*, 2023, **11**, 111090.
184 G. Hanbali, S. Jodeh, O. Hamed, R. Bol, B. Khalaf, A. Qdemat and S. Samhan, *Materials*, 2020, **13**, 3329.
185 P. Ndagijimana, X. Liu, Q. Xu, Z. Li, B. Pan and Y. Wang, *Sep. Purif. Technol.*, 2022, **299**, 121681.
186 B. Chenarani and M. N. Lotfollahi, *Mater. Chem. Phys.*, 2024, **322**, 129506.
187 M. Stachowiak, M. Cegłowski and J. Kurczewska, *Int. J. Biol. Macromol.*, 2023, **251**, 126356.
188 A. Eslami, M. Rafiee, R. Sedghi, A. Aliyari and B. Heidari, *Int. J. Environ. Anal. Chem.*, 2024, **104**, 7699–7721.
189 I. Mohiuddin, R. Singh and V. Kaur, *Int. J. Biol. Macromol.*, 2024, **269**, 131765.
190 L. K. Njaramba, M. Kim, Y. Yea, Y. Yoon and C. M. Park, *Chem. Eng. J.*, 2023, **452**, 139426.
191 K. A. Alibrahim, *J. Mol. Recognit.*, 2023, **36**(7), e3015.
192 S. Kim, F. Gholamirad, M. Yu, C. M. Park, A. Jang, M. Jang, N. Taheri-Qazvini and Y. Yoon, *Chem. Eng. J.*, 2021, **406**, 126789.
193 F. Mansouri, K. Chouchene, A. Wali, J. Labille, N. Roche and M. Ksibi, *Chemosphere*, 2024, **353**, 141469.
194 M. Obradović, A. Daković, D. Smiljanić, M. Ožegović, M. Marković, G. E. Rottinghaus and J. Krstić, *Microporous Mesoporous Mater.*, 2022, **335**, 111795.
195 J. L. Malvar, J. Martín, M. D. M. Orta, S. Medina-Carrasco, J. L. Santos, I. Aparicio and E. Alonso, *Appl. Clay Sci.*, 2020, **189**, 105529.
196 A. I. Osman, A. M. Elgarahy, N. Mehta, A. H. Al-Muhtaseb, A. S. Al-Fatesh and D. W. Rooney, *ACS Sustain. Chem. Eng.*, 2022, **10**, 12433–12447.
197 S. Fawzy, A. I. Osman, N. Mehta, D. Moran, A. H. Al-Muhtaseb and D. W. Rooney, *J. Clean. Prod.*, 2022, **371**, 133660.
198 E. C. Lima, A. Hosseini-Bandegharaei, J. C. Moreno-Piraján and I. Anastopoulos, *J. Mol. Liq.*, 2019, **273**, 425–434.
199 H. N. Tran, E. C. Lima, R.-S. Juang, J.-C. Bollinger and H.-P. Chao, *J. Environ. Chem. Eng.*, 2021, **9**, 106674.
200 E. C. Lima, A. Hosseini-Bandegharaei and I. Anastopoulos, *J. Mol. Liq.*, 2019, **280**, 298–300.
201 M. R. Cunha, M. Naushad, M. Ponce-Vargas, E. C. Lima, F. Sher, N. Rabiee, D. S. P. Franco, P. S. Thue, H. Nguyen Tran and M. Badawi, *J. Mol. Liq.*, 2023, **386**, 122470.